Alkali-activated materials produced using high-calcium, high-carbon biomass ash

Thiago H. Silva[a], Luis F.S. Lara[a], Guilherme J. B. Silva[b], John L. Provis[c], and Augusto C.S. Bezerra[a*]

[a] Federal Center for Technological Education of Minas Gerais, Belo Horizonte, Brazil

[b] Federal University of Ouro Preto, Ouro Preto, Brazil

[c] Department of Materials Science and Engineering, Sir Robert Hadfield Building, The University of Sheffield, Sheffield S1 3JD, United Kingdom

[*]Corresponding author: augustobezerra@cefetmg.br

ABSTRACT

Eucalyptus ash (EA) was used in this study as a high calcium ash (HCA) precursor for alkali-activated binders. The EA used also has high carbon unburned (High loss on ignition). This type of ash is one of the waste products from biomass-fuelled thermoelectric plants, and annually thousands of tons are discarded as a by-product of the energy generation process in Brasil, but it is rich in unburnt carbon which means that it is challenging to use in cementitious systems. Eucalyptus is a biomass that removes CO_2 from the atmosphere by photosynthesis and part of this carbon content remains in the ashes, generating CO_2 capture when EA is incorporated in the production of alkali-activated binders. The objective of the present study was to evaluate the properties of the material obtained by the alkali-activation of the high-calcium high-carbon biomass ash to generate a cementitious binder, with different pastes proportions of EA and silica fume (SF), activated by sodium hydroxide. With the different pastes, mortars were produced using standardized sand. The results obtained from the pastes and mortars were satisfactory in several aspects. The mechanical results of the alkali-activated mortars were comparable those of Portland cement mortars. Mortars degraded methylene blue more efficiently in illuminated conditions, even after high adsorption for 24 hours in the dark. The content of leached ions in the remaining solutions met potability standards.

Keywords: biomass ash, alkaline activation, cement, footprint, sustainability

1. Introduction

Eucalyptus is the most cultivated hardwood in the world. With about 20 million hectares planted in more than 100 countries throughout six continents, it is the main reforestation wood [1]. In 2016, the 7.84 million hectares of trees planted in Brazil were responsible for the stock of approximately 1.7 billion tons of carbon dioxide equivalent (CO_2 eq) and Brazil has 5.7 million hectares planted with eucalyptus, representing 72.7% of the area of forest plantations [2]. Among the destinations of reforestation wood and its residues, one important application avenue is its use as a biomass fuel [3]. In 2016, 47 million cubic meters (~23.5 million tonnes) of eucalyptus were used as industrial firewood in Brazil, 30.5% of all eucalyptus consumption for industrial use [2]. Some scenarios present the use of biomass for energy production as an effective way of capturing and removing CO_2 from the atmosphere [4]. Especially, the use of forest wood has been identified as a potentially major source of biomass energy in several studies (up to about 115 EJ.yr^{-1} in 2050) [5]. In addition, the thermal energy generation cost of fossil fuels is at least 34% higher than eucalyptus woodchip [6].

The burning of eucalyptus wood as sole fuel in a boiler generates up to 0.5% [7] of calcium rich ash [8]. Several biomass ashes rich in amorphous silica, such as rice husk ash and sugarcane bagasse ash, have been identified to have great potential as supplementary cementitious materials (SCMs) [9–11]. However, unlike these ashes, eucalyptus ash has a low percentage of silica [8], so it will not react as a pozzolan in Portland cement blends; in a recent review of the literature on vegetable ashes as a supplementary cementitious material, EA was not cited as a major possibility [12].

However, due to its high calcium content, one destination for the EA could be its use as a constituent in the production of alkali-activated materials, which can be produced from calcium-rich ashes [13–15], even though the low SiO_2 content of eucalyptus ashes will require a supplementary source of silica. Alkaline activation is the generic term applied to the reaction of a solid aluminosilicate (precursor) under alkaline conditions (induced by the alkaline activator) to produce a hardened binder, which constitutes a combination of hydrous alkali- or alkali earth-aluminosilicate phases [13].

Alkaline activator influences important properties of alkali-activated materials. Solid alkaline activators for the production of one-part alkali-activated materials with HCA change the compressive strength, fluidity and setting time [16]. Studies evaluating mechanical properties, shrinkage, and heat evolution of alkali activated with HCA identified a false set. However, the shrinkage of concrete tended to decrease with increasing NaOH concentration and the heat evolution of alkali-activated fly ash concrete was found to be two times lower than that of concrete made from Ordinary Portland cement at the same compressive strength [17]. Drying shrinkage, strength and microstructure of alkali-activated high-calcium fly ash using FGD-gypsum and dolomite as expansive additive was studied and changes in the properties studied were noticeable [18]. Strength and durability were studied in alkali-activated materials with HCA and waste marble aggregates, and the mechanical behavior was adequate, but the durability was impaired in some requirements [19].

HCA was used in alkali-activated repair material for concrete exposed to sulfate environment. HCA in alkali-activated material improved the compressive strength and provided lower mass losses by immersion in $MgSO_4$ solution compared to low calcium systems [20]. HCA was also evaluated in low cost and sustainable repair material made from alkali-activated high-calcium fly ash with calcium carbide residue. This study evaluated the bond strength of the alkali-activated mortar with concrete substrate, setting time of mortar and strength development. The setting time and strengths complied with the requirement of the ASTM standards for repair materials and thus indicated its suitable as an alternative repair material in terms of environmentally friendly and low cost [21].

The HCA in polypropylene (PP) fiber reinforced alkali-activated was evaluated at elevated temperature and the pastes with HCA and PP had improved mechanical behavior compared to the control with only HCA [22]. Pavement materials with low strength were studied by alkaline activation of HCA and mixtures with 20% HCA were recommended for pavement applications. [23]. Paving blocks were also produced by alkali-activation of HCA and met the requirements of standards [24]. Compacted earth blocks produced from the alkali-activation of iron ore tailings and HCA also showed satisfactory results [25].

Studies with the use of HCA in low carbon materials obtained by alkali-activation have already been developed. The analysis of low carbon materials with HCA showed the reduction of environmental impact when compared to Portland cement [26]. A downside of alkali-activated materials based on high unburned carbon content fly ash is carbonation and corrosion of reinforcement in structural applications [27]. It is expected that the use of HCA with high unburned carbon content (High loss on ignition) in the production of alkali-activated materials will trap carbon in the structure of these materials, making them even more sustainable.

The hydraulically active high calcium coal fly ashes described in the literature [14,15] tend to have around 30% CaO, with the sum of $SiO_2 + Al_2O_3 + Fe_2O_3$ exceeding 50% to enable compliance with the historical provisions of the ASTM C618 Class C specification. However, considering the much lower content of these major oxides, and the high CaO and unburnt carbon contents of the EA tested here, the present study evaluates the potential of this high-calcium high-carbon biomass ash to react with an alkaline solution in the presence of an additional source of reactive silica for the production of a cementitious binder material; the potential of this binder to promote degradation of organic pollutants was also assessed. The degradation of organic pollutants was evaluated by evaluating the degradation of methylene blue solution under conditions without and with UV lamp lighting. The experiments indicated a greater degradation of the methylene blue dye under UV illumination, even without the use of semiconductor particles, presenting a phenomenon analogous to photocatalysis.

2. Materials and methods

2.1 Materials

To verify the possibility for the use of EA to produce an alkali-activated binder material, silica fume (SF) was used. Although SF has limited production in the world [28] and is used in high performance cements and concretes in relatively low percentages from 5 to 10% [29], it was selected for the present study due to its high content of silicon oxide and its high reactivity with calcium hydroxide [30,31]. SF was provided by Tecnosil Indústria e Comércio de Materiais de Construção Ltda; it is obtained from the manufacturing process of silicon metal or iron silicon in Dow Corning Metais of the Pará Indústria e Comércio Ltda. Brazil

is the second largest producer of silicon metal, behind only China. It is also the second largest exporter of

silicon metal and ferrosilicon to the United States [32] The EA was collected on the boiler filter from Nestlé

SA in Brazil. Nestlé buys eucalyptus logs and cut them into chips, which are free from peels and leaves.

The chips are burned in a boiler to generate steam for the milk dehydration process and to generate energy

for the industry. The filter employed does not use water, thus the ash was collected completely dry. The as-

received EA was ground in a high-performance planetary mill at 300 rpm [33], in 500mL containers with

ZrO_2 and 25 zirconia oxide spheres of 20 mm diameter for 10 min (after time trials of 2, 4, 6, 8, 10, 12 and

20 min, and use of spheres with diameters of 10, 15 and 20 mm), to reduce its particle size. Chemical

composition by XRF, loss on ignition at 1000°C (LOI) [34], particle density, particle size distribution after

grinding, surface area and pore volume of the EA and SF are shown in Table 1. The chemical composition

of the EA was determined by the lithium tetraborate fusion method and quantification in an energy

dispersive X-ray fluorescence spectrometer (XRF) Panalytical Axios Fast. The EA presents predominantly

CaO in its chemical composition [8,24], followed by MgO, and has a high loss on ignition [24].

Table 1: Properties of the EA and SF

	EA	SF
Chemical composition by XRF (wt%)		
SiO_2	1.76	94.95
Al_2O_3	5.06	0.70
Fe_2O_3	2.43	0.12
CaO	43.80	0.99
MgO	8.36	-
TiO_2	0.53	-
P_2O_5	3.32	-
Na_2O	0.28	-
K_2O	4.64	2.84
Loss on ignition (1000 °C)	29.72	0.37
Particle density (g/cm^3)	1.98	2.20
Particle size distribution		
D_{10} (µm)	1.86	0.34
D_{50} (µm)	8.97	1.52
D_{90} (µm)	24.35	9.78
Surface area by Multipoint BET method (m^2/g)	13.84	8.55
Micropore volume (cm^3/g)	6.106×10^{-3}	4.268×10^{-3}

Through the visual analysis of EA presented in Figure 1 (a), it is possible to observe powdery particles of a light grey colour, which indicates a low amount of unburned organic matter in relation to the rest of the sample; while the elongated particles in dark grey colour indicate the presence of carbon fibres with high carbon content due to incomplete combustion. In Figure 1 (b) it can be observed that after the comminution process, the EA appears more uniform in both colour and particle size.
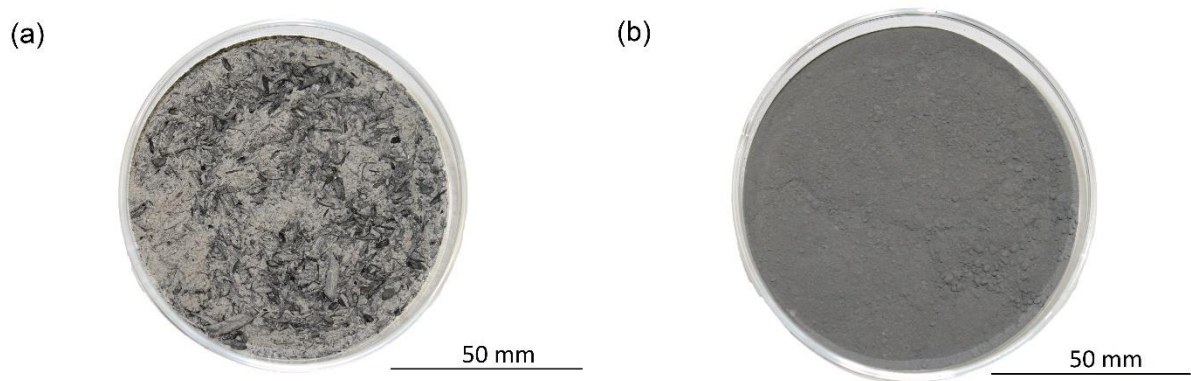

Fig. 1: (a) EA as-received (b) ground EA

To evaluate the EA morphology, it was imaged using a Hitachi TM 3000 scanning electron microscope (SEM) under low vacuum conditions with backscattered electron detectors (BSE) and acceleration voltages of 5 and 15 kV [35]. For analysis by energy dispersive spectroscopy (EDS), a Shimadzu SEM and EDS analyser with 30 mA filament current, 25 kV voltage and gold-coated samples were used. Figure 2 shows three images obtained by SEM analysis of the EA. Particle (a) presented a spherical shape, and Ca, K, Cl, O, C and Mg were detected by EDS. Particle (b) is possibly a fibre that did not completely burn during the process in the boiler of the thermoelectric, and its composition in terms of detected chemical elements was 71% C balanced by O, K, Ca and Mg. Particle (c) is a grain of non-regular geometry and an apparently rough surface, with Ca, O and Mg. The SF presented a typical spherical structure as identified in the literature.
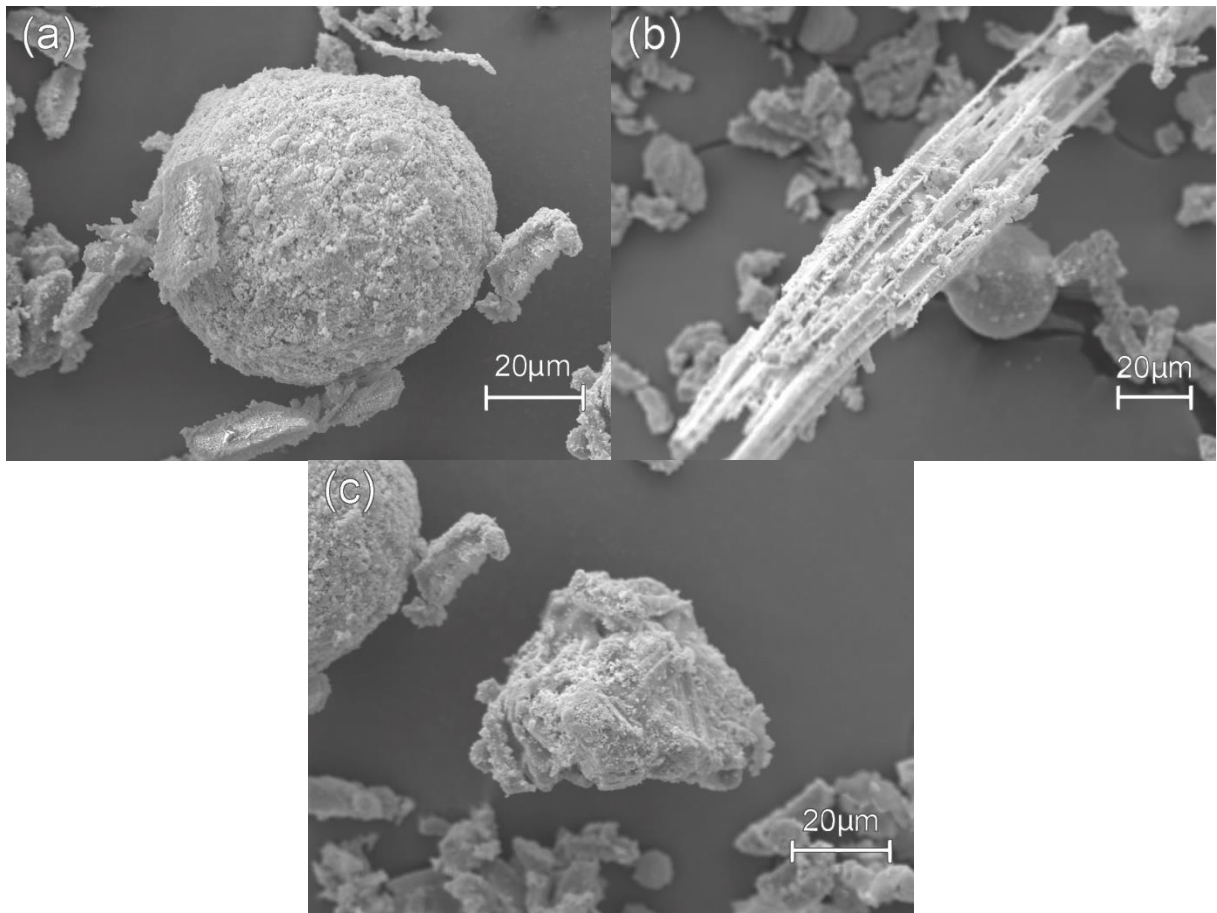
6

Fig. 2: SEM images of EA as received

The high loss on ignition may be due to the incomplete combustion of eucalyptus fibres as shown in Fig 2 (b), as well as dehydroxylation and decarbonation to form CaO and MgO phases. An important aspect is that although the SF is finer than the EA by particle size analysis, the EA presented a larger BET surface area. This is likely due to the EA presenting a rougher lamellar surface and high-surface area porous unburned carbonaceous matter, which corroborates the results of pore volume analysis. The small particle size and high surface area of the EA can lead to high reactivity, even with a relatively crystalline structure [36]. Based on the contents of calcium and silicon in the EA and SF, the 60EA40SF, 50EA50SF and 40EA60SF pastes presented Ca/Si ratios of approximately 0.70, 0.45 and 0.30, respectively.

Figure 3 shows the diffractograms of the EA and SF, it is possible to identify crystalline peaks of calcite - $CaCO_3$, Crystallography Open Database (COD) 4502441 [37]; lime - CaO (COD 7200686) [38]; periclase - MgO (COD 9006806) [39]; sylvite – KCl (COD 9003115) [40]; and portlandite - $Ca(OH)_2$ (COD 1529752) [41]. The XRD analysis also indicated traces of moissanite 3C – SiC (COD 1010995) [42] and

silicon – Si (COD 4507226) [43] in the SF. The presence of portlandite was not expected at EA, as it is an ash obtained by burning eucalyptus in a boiler, filtered, collected and stored dry in a closed container. However, due to the high reactivity of lime (CaO), it is believed that during the handling of EA in the laboratory, part of the lime reacted with the humidity of the air causing the formation of portlandite.
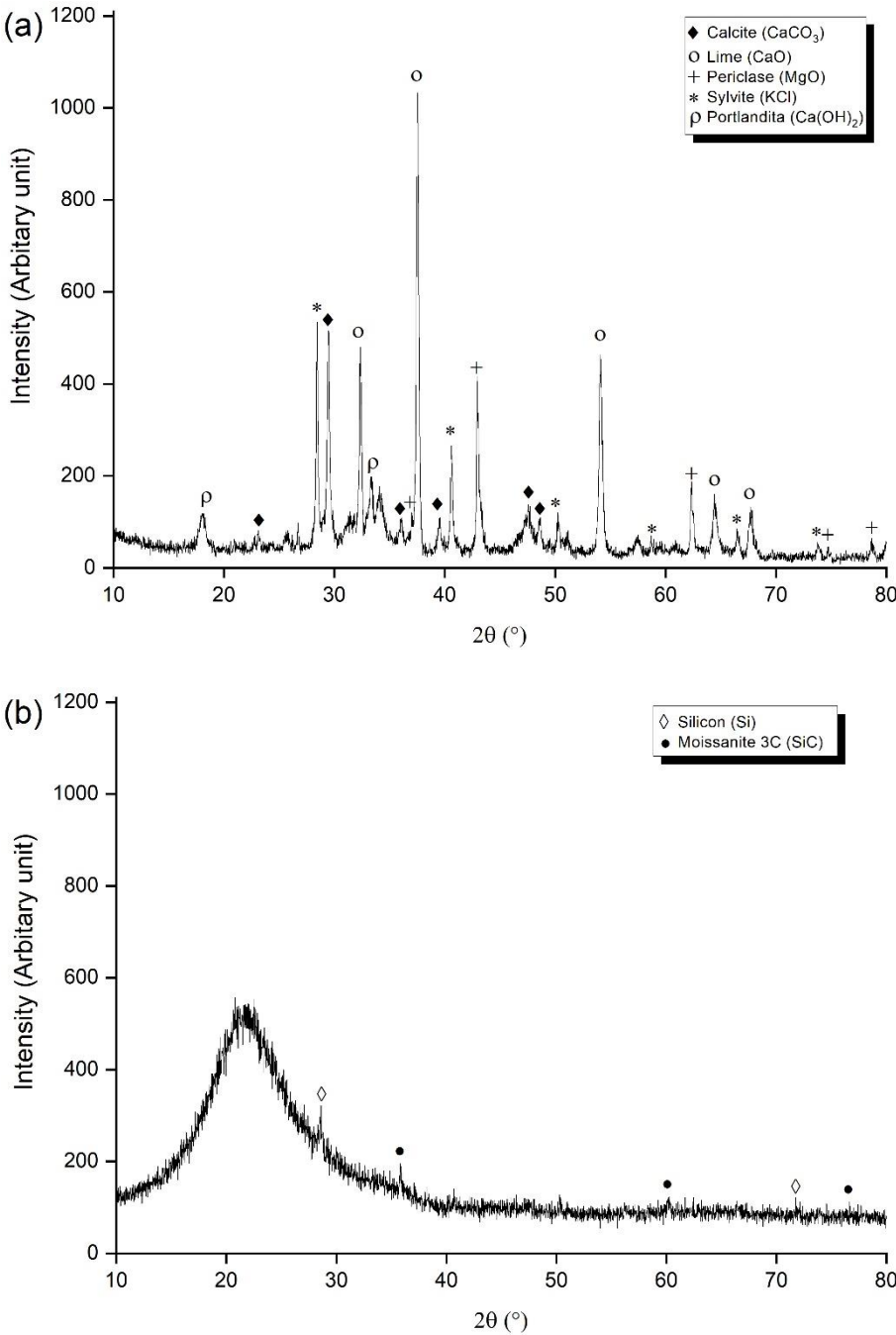

Fig. 3: XRD of (a) EA and (b) SF

Figure 4 shows the curves obtained in thermal analysis of EA. It is believed that mass losses up to 400°C occur due to dehydration and decarbonation of calcium oxalates, depolymerization of the partially-combusted hemi-cellulose and lignin residues in unburnt wood fibres within the EA [44–47]. Between 400 and 450 ºC it represents the decomposition temperature of portlandite - $Ca(OH)_2$ [48–50]. From 600 to 800ºC the decomposition of the carbonate $CaCO_3$ leads to the formation of CaO and CO_2 [51,52].
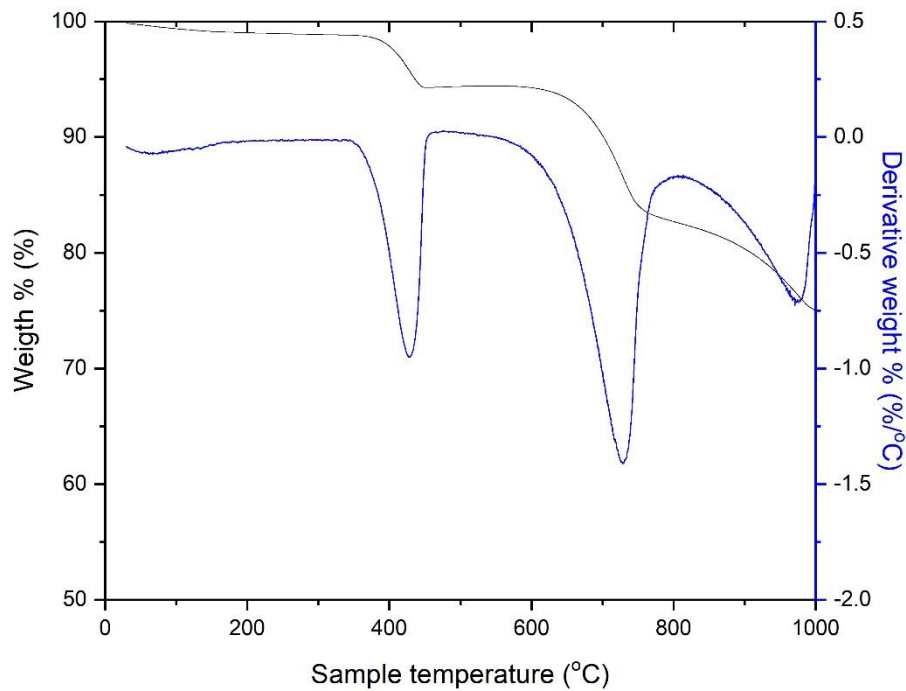
Fig. 4: TGA and DTG of the EA

2.2 Methods

The hardened pastes were ground to below 45 μm and immersed in isopropanol for 15 min. Afterwards, the samples were dried at 40°C. The crystalline phases in the ash and resultant binders were identified through X-ray diffraction using a D2 Phaser (Bruker), with a copper X-ray tube operated at 30.0 kV and 10.0 mA and Ni-filter, set to 0.018° 2θ sweep per step, from 8 to 70° at 1.0 s/step. For the Rietveld refinements, the program Topas version 5.0 was used. The PONKCS method was used in combination with the internal standard method to obtain a quantification of calcium silica hydrate (C-S-H) and the degree of reaction of SF. A phase model for SF was created using 50/50% mixture with a griceite standard (LiF/SF), a Pawley fit within the lattice parameters a = 1 nm; c = 70 nm, and the space group P4 [53,54]. The phase

9

constant "ZMV" was determined by the internal standard method as in [53]. The procedure outlined by Bergold et al. [55] was used for calibrating the C-S-H phase and determining its phase constant, applying the Pawley fit model within the lattice parameters of a 14 Å tobermorite [56]. The Chebyshev polynomial of 2nd order combined with a $1/2\theta$ term was used to fit the background intensity.

A Shimadzu DTA-60H thermal analyser with 5ºC/min heating rate and 1200ºC maximum temperature was used for the differential thermal analysis (DTA) and the thermogravimetric analysis (TGA), operated with nitrogen gas at 50 mL/min. Particle size distribution was determined using a CILAS 1090 Laser Particle Size Analyser apparatus, with particle dispersion by ultrasound for 240 seconds and 15% obscuration. The surface area of the samples was determined by N_2 sorption on a Quantachrome Nova 2200 with 9 mm bulb, after heat treatment at 100°C for 60 minutes of degassing.

Pastes containing different proportions of EA, SF and sodium hydroxide solution were prepared with an activation solution-to-solids mass ratio (a/s) of 0.5 (Table 2). The sodium hydroxide solutions were employed at concentrations of 5, 10 and 15 mol/L. Pastes were cast into non-sealed steel moulds and cured at 24°C with air humidity between 50-60%.The pastes were characterised by scanning electron microscopy, X-ray diffraction, surface area, porosimetry and compressive strength at 28 days. Compressive strength by testing five replicate cylindrical specimens of 25 mm diameter and 50 mm height.

To perform the SEM images of the folders, two types of equipment were used. The samples were sawn to obtain cubic fragments with 10mm edges. The fragments were embedded in acrylic resin and after embedding, the pieces were sanded and polished. The samples were analyzed in scanning electron microscopy (SEM) model Hitachi TM-3000 under a low vacuum with a backscattered electron detector and electron acceleration voltage of 15 kV. These images were performed to obtain images with high resolution and with grayscale color differentiation for different phases. To obtain the chemical composition of the different phases, the embedded, sanded and polished samples underwent a surface metallization process with gold-coated. The metalized samples were analyzed using a TESCAN VEGA3 scanning electron microscope (SEM) under high vacuum-operated at 15kV and equipped with an Oxford EDS system.

Table 2: Paste mix designs

Sample ID	EA (%)	SF (%)	Solution concentration NaOH (mol/L)
60EA40SF 0M	60	40	0
50EA50SF 0M	50	50	0
40EA60SF 0M	40	60	0
60EA40SF 5M	60	40	5
50EA50SF 5M	50	50	5
40EA60SF 5M	40	60	5
60EA40SF 10M	60	40	10
50EA50SF 10M	50	50	10
40EA60SF 10M	40	60	10
60EA40SF 15M	60	40	15
50EA50SF 15M	50	50	15
40EA60SF 15M	40	60	15

With the same paste mix designs shown in Table 2, mortars were also produced, with a 1:3 dry mass ratio between the binder (EA+SF) and sand. The mortars were dosed with a high-range water reducing agent (plasticiser), MC POWERFLOW 1180 (MC - Bauchemie Brasil Indústria e Comércio Ltda), to yield similar workability and consistency for the various mixes, controlled by empirical observation. For the 60EA40SF mortars, a plasticiser/binder factor of 0.012 ± 0.001 was used; while for the 50EA50SF and 40EA60SF mortars, ratios of 0.016 ± 0.001 and 0.018 ± 0.001 were used respectively. Mortars were cast into non-sealed steel moulds and cured at 24°C with air humidity between 50-60%.

The mortars were categorised in terms of apparent density, porosity and water absorption by immersion according to NBR 9778 [57], and compressive strength by testing five replicate cylindrical specimens of 25 mm diameter and 50 mm height at the ages of 3, 7, 28 and 154 days. The loading speed of the testing machine, while transmitting the compression load to the paste and mortar specimens, was 0.25 ± 0.05 MPa/s [58,59]. The end surface preparation of compressive strength test specimens was an unbonded system using neoprene pads in metal retainer rings [60]. Specimens with noticeable expansion after curing, had the excess parts beyond the mould dimensions removed by sawing.

A property of some interest for new binders would be the ability to degrade organics, either to remove organic dyes from wastewater or even to produce self-cleaning facades [61]. Methylene blue (MB) was used as a model compound to evaluate the potential for organic pollutant degradation [62]. Cylindrical mortar specimens of 25 mm diameter and 50 mm height were immerged in 150 mL of distilled water

containing 20 mg/L MB, without agitation. The mean mass of the specimens was 35.2 ± 3.0 g. The MB degradation was evaluated under two lighting conditions for the same specimens, with the first 24 hours of degradation in a darkroom (no light); at the end of this first cycle the MB solution was replaced by a new solution of the same initial concentration, and the specimens placed for a further 24 hours in a chamber with 390×600×400 mm internal dimensions and two G15T8 UV-C 15 W lamps operated at 55 V, with 450mm length and 254 nm UV-C emission and UV power equal to 49 uW/cm^2 at 1 m. In order to eliminate the effect of MB's natural degradation under UV, a control solution was carried out that was not put in contact with the specimens.

A 5 mL solution aliquot was collected at the beginning of the test and then at 2, 4, 8 and 24 hours of each cycle, and light absorbance measurements were performed from 250 to 850 nm in a Lambda 1050 UV/Vis Spectrophotometer. The calibration curve was constructed with 1.25, 2.50, 5.00, 10.00 and 20.00 mg/L concentrations, and the 664 nm peak was used for quantification. The dye degradation tests were performed using samples that had been cured for 240 days, so that the main alkali-activation reactions were already finished and would not influence the degradation measurements. This option was chosen so that precursors and activators that could react over time would not be leached before reactions took place. After the degradation tests in the dark and illuminated phases, samples of the solutions of all the mortars were collected. Nitric acid (HNO$_3$) was added to the solutions until their pH was below 2, refrigerated at 5 °C until the time of testing, and these solutions were analysed by inductively coupled plasma atomic emission spectrometry (ICP OES) and inductively coupled plasma mass spectrometry (ICP-MS). After this cycle of degradation analysis of MB, the entire procedure was performed once more with the same test specimens.

3. Results and discussion

3.1 Characterization of pastes and mortars

The X-ray diffraction analysis of hardened pastes, Figure 5, revealed periclase (COD 1000053) and quartz (COD 9012600) in all hardened pastes. Periclase content ranged from 0.79% to 3.27% and quartz content ranged from 0.14% to 0.91%. Lime and hydrous Mg-rich phases were not identified; while the former was

hydrated to form C-S-H, periclase did not undergo significant hydration to form the brucite or other identifiable reaction products. The 0M-pastes and 5M-pastes presented calcite (COD 9009668); whereas in 10M and 15M-pastes, due to higher sodium content, the carbonate present was consumed by the sodium-rich pore fluid to form pirssonite $Na_2Ca(CO_3)\cdot2H_2O$ (COD 9009889) and thermonatrite $Na_2CO_3\cdot H_2O$ (COD 9011153) [63–65]. Quantitative phase analysis obtained through the PONKCS method is exhibited in Figure 6. As expected, C-S-H was the main hydration product of the alkali activated blends [66]; thereby, increasing the activator molarity above 5M resulted in significantly higher C-S-H content, and it decreased the occurrence of unreacted SF. In addition, the consumption of carbonates to form thermonatrite and pirssonite is evident as the activator molarity is increased to 10M and 15M. Pirssonite content increases from 10M to 15M, while thermonatrite is formed only under 15M conditions. Polymorphs of calcium carbonate were found in 0M-pastes; all of which presented traces of aragonite (COD 9016147) related to the carbonation of amorphous C-S-H [67], while only 40EACA60SF 0M showed traces of vaterite (COD 9007475).
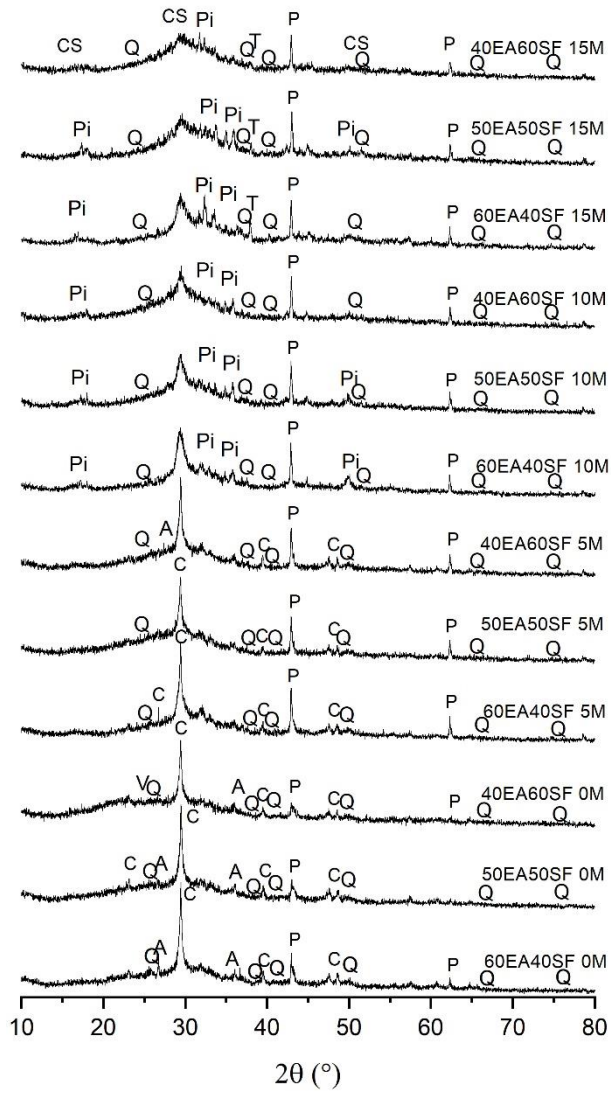
C- Calcite / CS- Calcium silicate hydrate / P- Periclase / Pi- Pirssonite
A- Aragonite / V- Vaterite / T- Thermonatrite / Q- Quartz

Fig. 5: XRD of the pastes
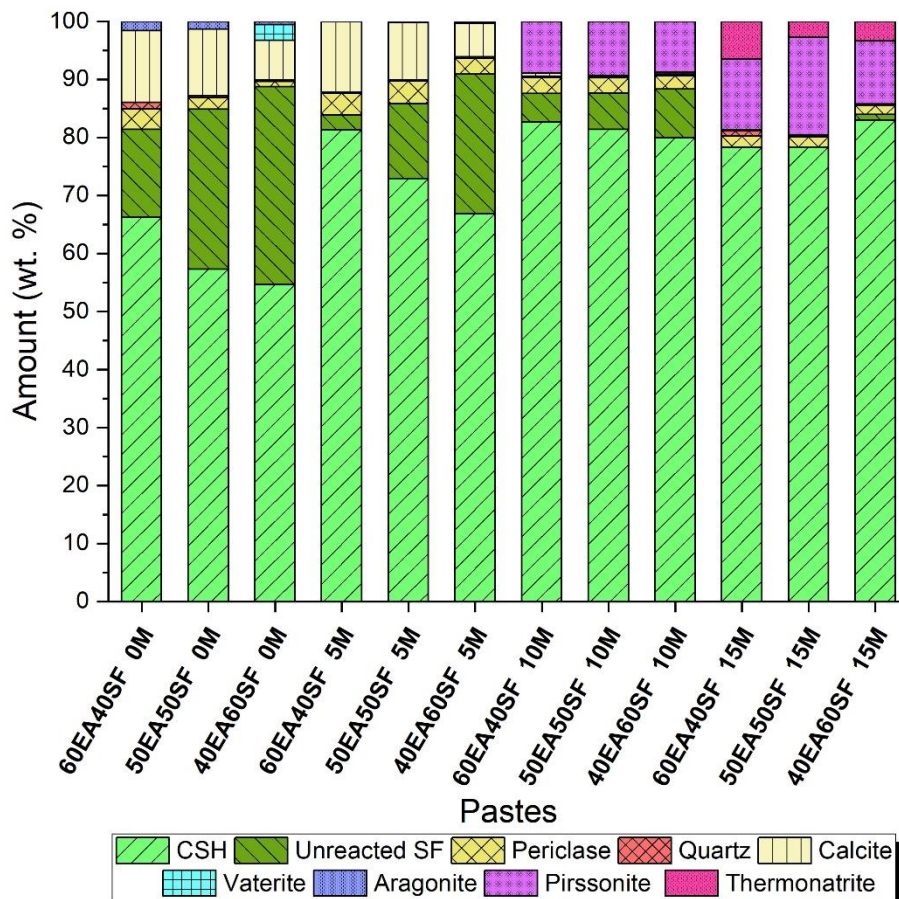
Fig. 6: Development of the absolute phase content in hydrating mixtures of EA and SF

Figure 7 shows photographs of the cylindrical specimens of 5M and 15M pastes. It is possible to observe that the specimens made with the 15M solution (d-e-f) presented visible expansions. It is believed that the larger expansions resulted in the cracks observed by SEM in Figure 8 (g) to (k). Although the group of specimens from the 5M and 15M pastes presented the same SiO_2/Al_2O_3 ratio for the same EA/SF ratios, the increase in the concentration of NaOH in the alkaline activator provided foam formation in a similar way to that detailed by [68]. Whereas with higher SiO_2/Al_2O_3 ratio, foaming process are predominant; in the 15M pastes, the 40EA60SF paste (with the highest amount of SiO_2, ie higher SiO_2/Al_2O_3 ratio) was the one that presented the greatest expansions. To cylindrical specimens of 15M pastes, a high sodium content in the mixtures results in carbonation reactions with the environment, which can generate efflorescence due to carbonated products on the surface of the samples [69].

Mortars made with the respective pastes also showed perceptible expansions, although to smaller extents, mainly due to the lower binder content as a proportion of the total mass of the specimens, and also to the relief of stress and absorption of deformations by the paste-aggregate interface.
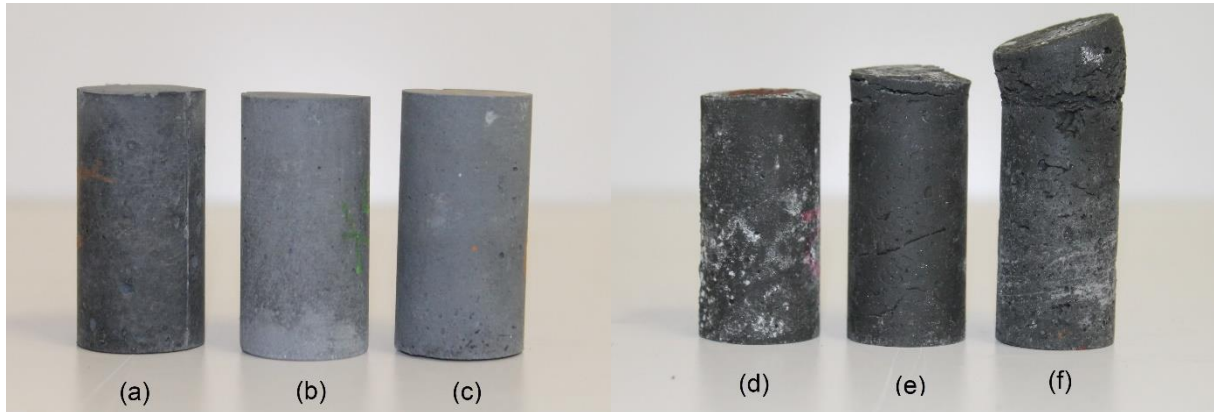

Fig. 7: Images of paste specimens, of original dimensions 25 mm diameter and 50 mm height.

(a) 60EA40SF 5M; (b) 50EA50SF 5M; (c) 40EA60SF 5M; (d) 60EA40SF 15M; (e) 50EA50SF 15M and (f) 40EA60SF 15M

Figure 8 shows the images obtained by SEM analysis of the pastes. In Figure 8 (a) there are several spots similar to point 1, which appears to be calcium carbonate [70–72] and the rhombohedral shape (Point 3) would indicate the polymorph is calcite [72]. Point 5 shows unreacted SF spheres. Points 2 and 4 are mainly C-S-H, and calcium aluminosilicate hydrate (C-A-S-H) with a smaller content [73–75]. Point 6 shows unreacted EA sphere. In Figure 8 (b), area 7 is similar to point 2 in Figure 7 (a), point 8 is similar to point 3, and point 9 is similar to point 1. Point 10 is likely to be unreacted SF spheres. In Figure 8 (c), it can be appreciated how points 11, 12, and 13 are similar to points 1, 3 and 2 respectively. Points 14, 15 and 16 are likely to be unreacted SF spheres In Figure 8 (d) point 17 is calcite, similarly to point 1. It is possible to observe unreacted SF spheres in point 19, similar to points 5 and 15, as well as the region 18 composed of calcium silicate hydrate, identical to points 7 and 13. In Figure 8 (e) some angular (Point 21) and spherical structures (Point 22) can be observed; these are typical of calcium carbonate and unreacted SF respectively. C-S-H can also be observed in point 20. Figure 8 (f) shows calcium carbonate (point 23) similar to points 1, 9, 11 and 17. Fully hydrated C-S-H (Region 24) can be seen in the rest of the image. In Figure 8 (g) to (l) a relatively more porous structure is observed (points 25, 28, 30, 32 and 34), when compared to images

(a) to (f), with the presence of cracks (26, 27, 29, 31, 33 and 35). Figure 8 (l) illustrates a gel structure (36), which could be the cause of expansions, especially if this a gel of hygroscopic nature, which could have been formed by alkali-silica reaction [76]. Structures of crystals (Point 37) and foam can be seen in Figure 8 (m) and (n). In Fig. 9 four images are shown with the EDX of some phases. It is possible to notice that Figures 9 (c) and (d) (compared to Figures 9 (a) and (b)) have the surface becomes smoother and more homogeneous caused by the higher degree of reaction caused by the increase in NaOH concentration [77], which leads to greater strengths [78].

30 um

30 um

30 um

30 um

30 um

30 um

18
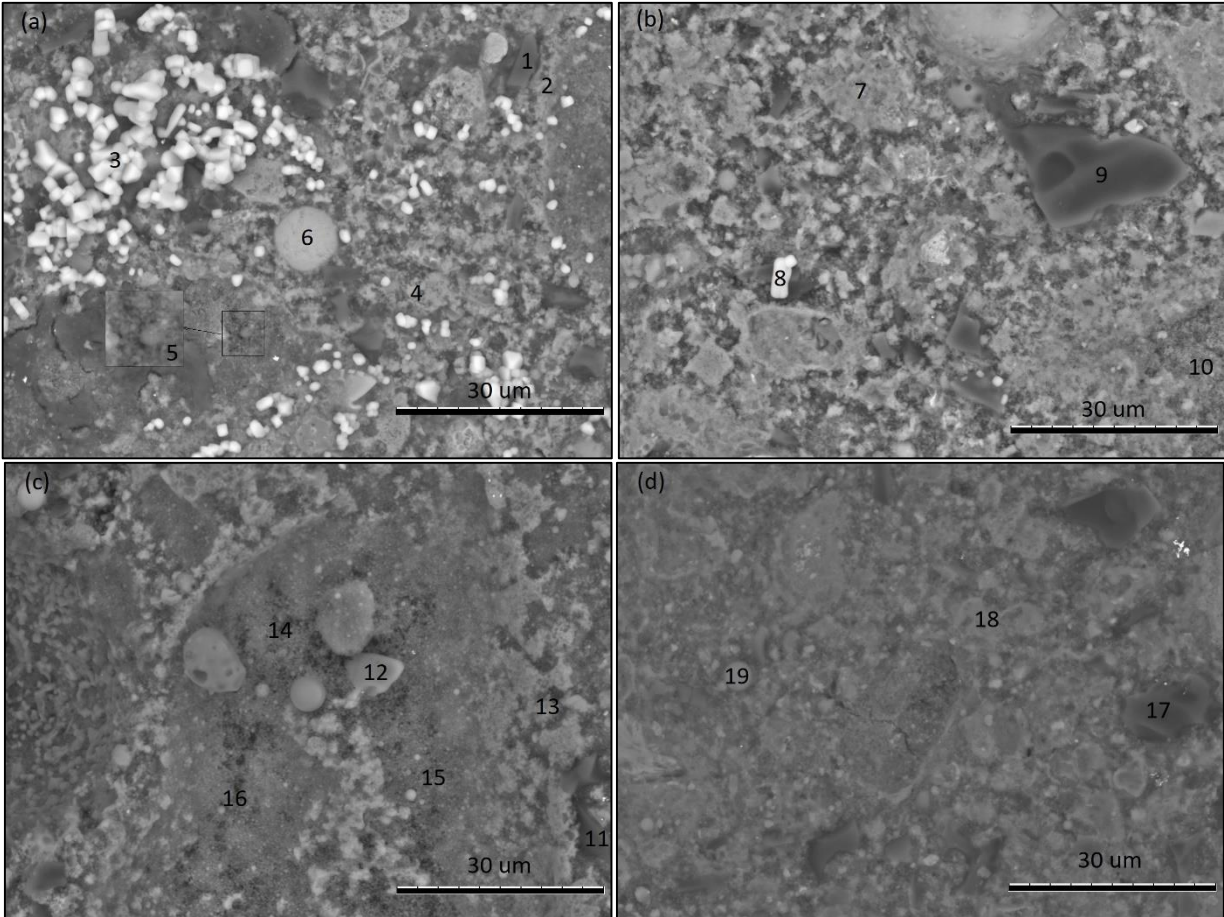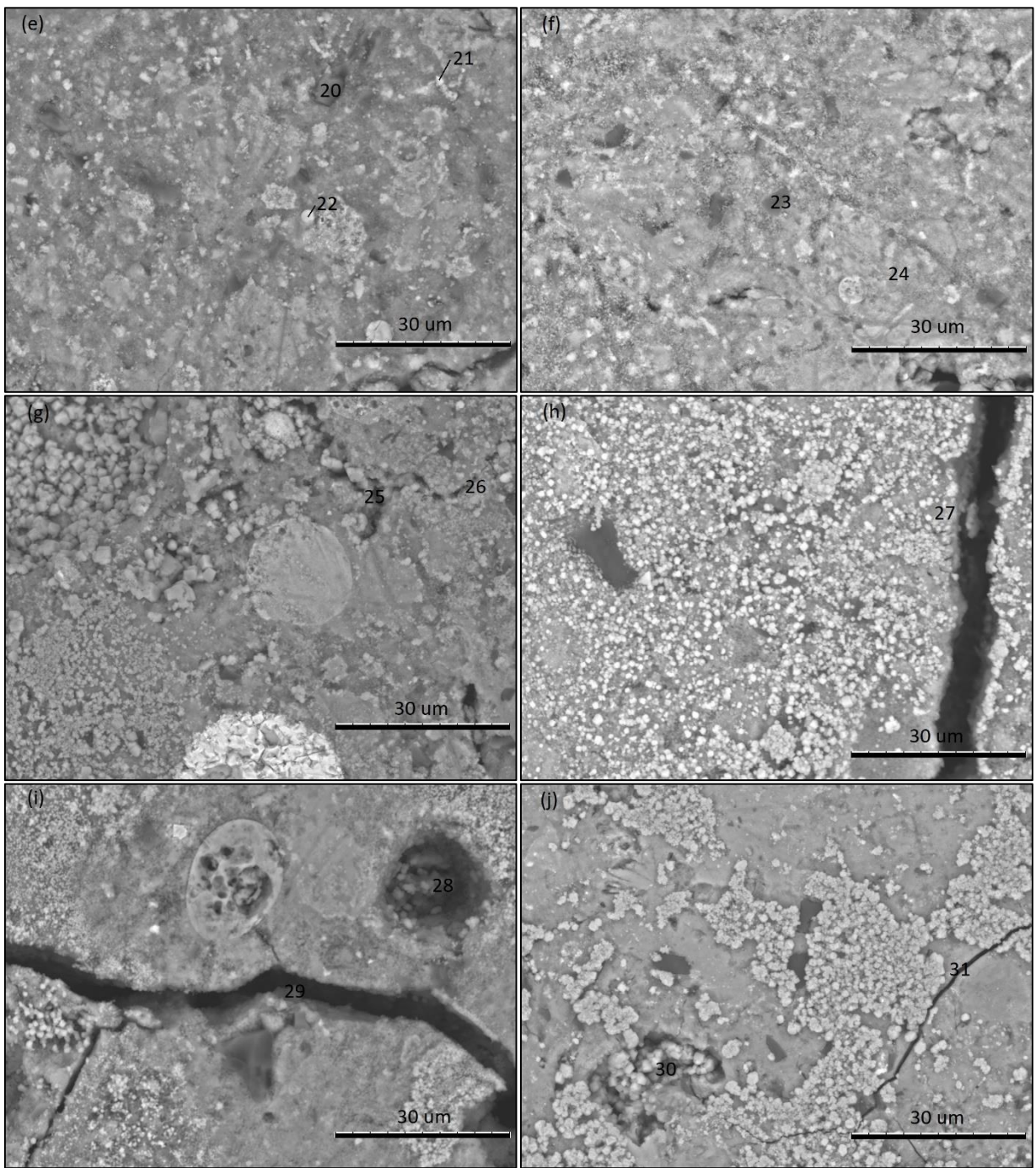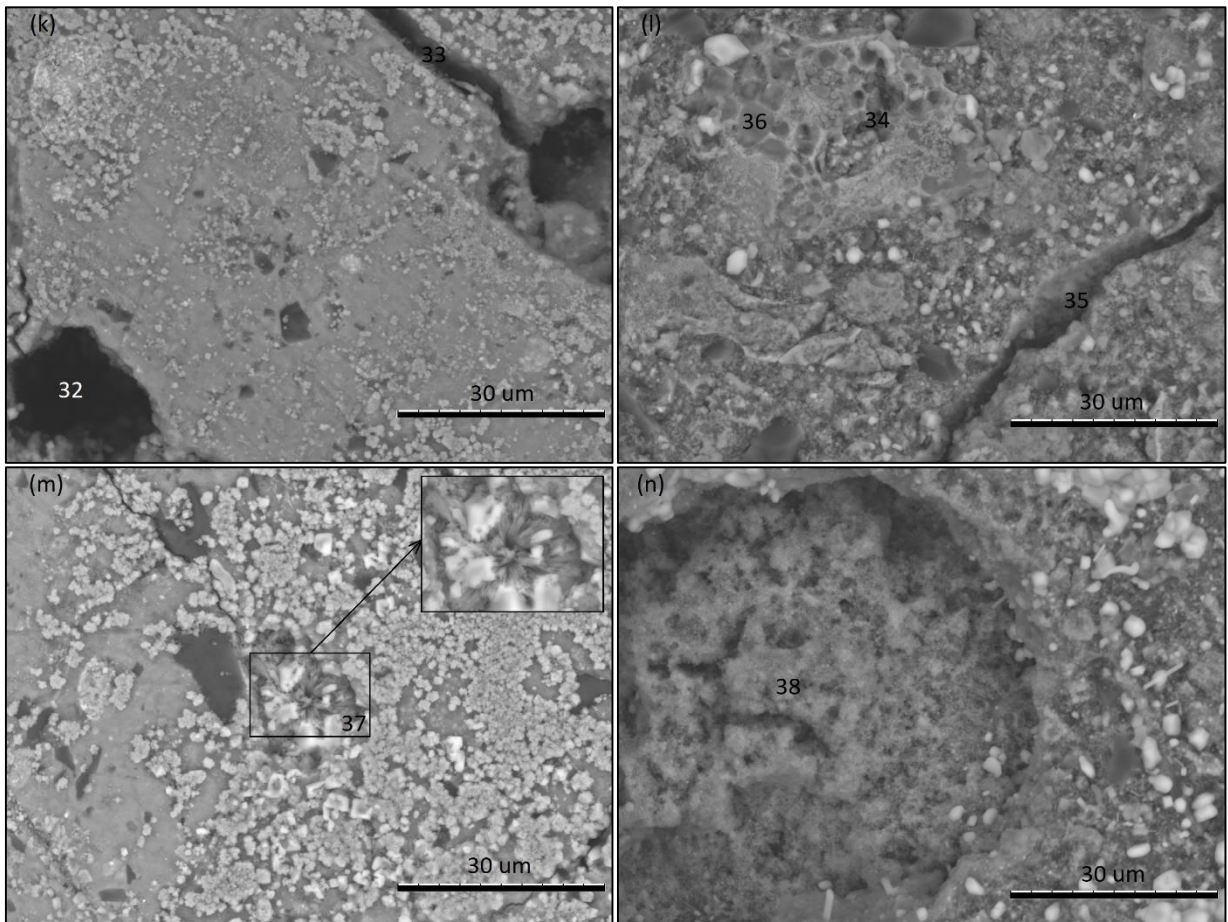
Fig. 8: SEM images of pastes.

(a) 60EA40SF 0M; (b) 50EA50SF 0M; (c) 40EA60SF 0M; (d) 60EA40SF 5M; (e) 50EA50SF 5M; (f) 40EA60SF 5M;

(g) 60EA40SF 10M; (h) 50EA50SF 10M; (i) 40EA60SF 10M; (j) 60EA40SF 15M; (k) 50EA50SF 15M, (l) 40EA60SF 15M;

(m) 60EA40SF 15M and (n) 40EA60SF 15M
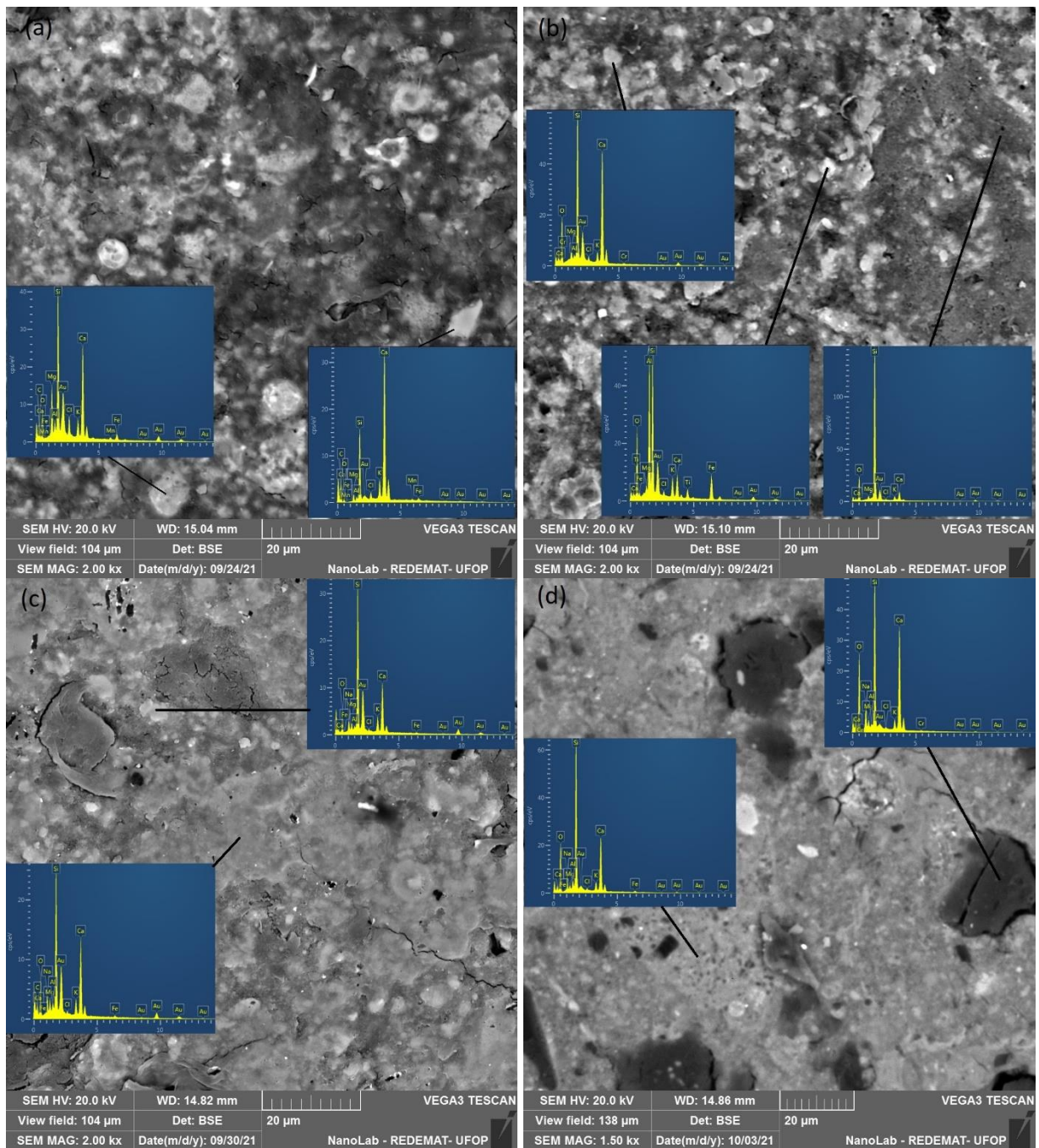
Fig. 9: SEM images of pastes with EDS.
(a) 60EA40SF 0M; (b) 40EA60SF 0M; (c) 60EA40SF 0M; (d) 40EA60SF 0M;

Figure 10 shows physical and mechanical properties of the hardened pastes. It can be observed that the pastes with lowest pore volume were those prepared using the alkaline activator solution at 15 mol/L, independent of the EA and SF proportions. From the point of view of durability, it will be interesting if this reduction in the pore volume has occurred, as it would reduce the exposure to deleterious agents and therefore provide a longer service life. However, when correlating: (i) the occurrence of macroscopic

expansion after moulding, (ii) the decrease in peak intensity for the crystalline phase in the diffractograms of the pastes with higher concentrations of sodium hydroxide solution, (iii) the presence of fissures visualised by scanning electron microscopy, and (iv) the presence of apparently non-crystalline structures visualised by SEM; it is understood that the 15M concentration was responsible for the formation of expansive constituents; which are capable of reducing porosity by filling pores in the range evaluated, while causing significant expansion.

As for the mechanical behaviour, in general, a gain of strength can be identified with the use of sodium hydroxide solution at 5 mol/L when compared to the 0M mixes that did not use an alkaline activator solution. The higher compressive strength in 5M pastes was concomitant with the increase of amorphous phase C-S-H. However, higher NaOH concentrations (10 and 15 M) did not result in further formation of C-S-H despite a higher SF 'consumption', which could be related to decalcification of C-S-H and formation of hydrated layers on the surface of partially reacted SF particles [79]. For the 10M and 15M samples, the low strength is probably due to the excess of alkaline ion, which makes it difficult for Si and Ca ions to condensate to form the gels. An increase in the Na/Si ratio is correlated with a decrease in the amount of silica, while a lower Na/Si ratio is achieved with a higher amount of silica and lower amounts of NaOH. It is known that an increase in the alkalinity of the paste can affect the polymerization process. The incorporation of silica in these pastes is low, making it difficult to form gels that provide strength to the material [69,80,81].
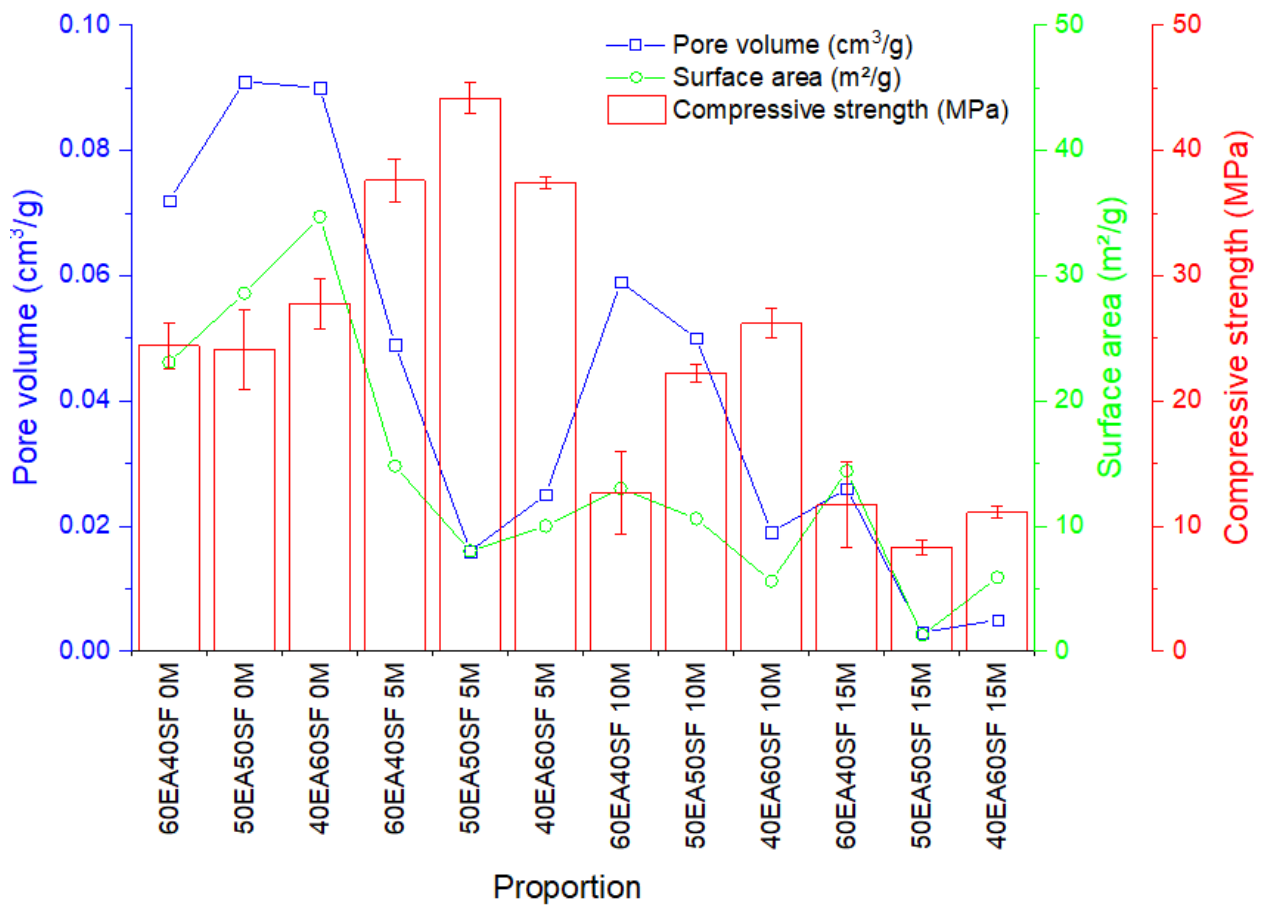
Fig. 10: Physical and mechanical properties of pastes at 28 days

Table 3 shows physical properties of the mortar specimens. As anticipated, the physical properties of mortar specimens were consistent with properties of the pastes. In general, the pastes that presented larger pore volumes led to mortars with higher porosity and water absorption. The results of physical properties of the mortars are consistent with results of other alkali-activated materials and Portland cement mortars. Comparing with alkali-activated pastes with high carbon ash, the results obtained for porosity are equivalent or lower, water absorption are lower and apparent density are equivalent. [33]. For alkali-activated mortars in general, the porosity, water absorption and bulk density values are equivalent [82,83]. Comparing with Portland cement mortars with supplementary cementitious material insertion, the porosity and water absorption results are equivalent [58,84].

Table 3: Physical properties of mortars

Proportion	Porosity (%)	Water absorption (%)	Apparent density (g/cm³)
60EA40SF 0M	21.9	9.9	2.22
50EA50SF 0M	22.4	10.0	2.23

40EA60SF 0M	22.4	10.5	2.12
60EA40SF 5M	17.8	7.3	2.44
50EA50SF 5M	18.5	7.8	2.37
40EA60SF 5M	20.1	9.2	2.19
60EA40SF 10M	17.6	7.8	2.24
50EA50SF 10M	15.9	7.3	2.17
40EA60SF 10M	16.3	7.4	2.21
60EA40SF 15M	13.8	6.5	2.13
50EA50SF 15M	18.5	8.6	2.17
40EA60SF 15M	15.8	7.0	2.27

Figure 11 presents the compressive strength results of mortar specimens. All mixes with 5 mol/L sodium hydroxide solution yielded mortars that obtained a compressive strength above 55 MPa at 28 days. Mortars 50EA50SF 10M and 40EA60SF 10M may be added to this group, while 60EA40SF 10M mortar presented considerably lower compressive strength. The mortars produced with the 15 mol/L solutions resulted in the lowest values of compressive strength. Mortars produced with the 0 mol/L solutions displayed compressive strengths close to 30 MPa at 28 days. The mortars exhibited a compressive strength at 154 days slightly higher than that at 28 days, except for 40EA60SF 0M mortar, which experienced a decrease in strength at this more advanced age.
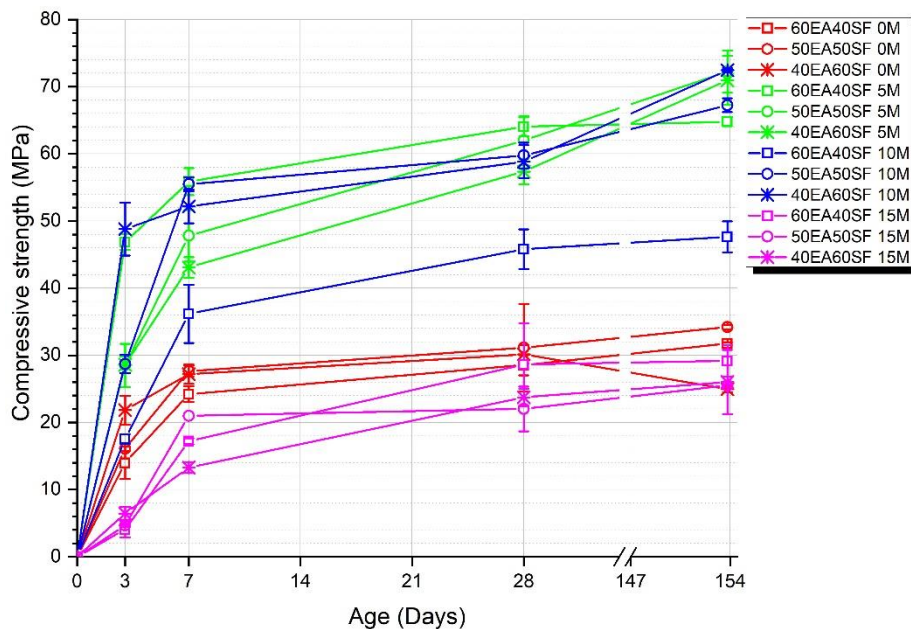

Fig. 11: Compressive strengths of mortars

The alkali-activated materials produced with 5M and 10M reached compressive strength greater than 34 MPa at 7 days, strength required as a requirement of high initial strength Portland cement [85]. The

compressive strength values obtained for the alkali-activated materials produced with 5M and 10M are higher than those stipulated in the international standard ASTM C1157 for various types of cement, including hydraulic cement for construction (28 MPa) and high sulfate resistance cement (25 MPa) [86].

Comparing the results of compressive strength of pastes and mortars with the same proportions of EA and SF, it can be seen that the results of compressive strength of mortars are substantially superior to the results obtained by the pastes. Compressive strength test results for specimens with the same geometry, Portland cement mortars show 32% higher results than pastes [87]. Compressive behaviours of cement-based materials are sensitive to strain rate [88]. In high strain rate loading, concrete specimens failed with comparatively less violence than cement paste and mortar, however, for a static compressive stress–strain curve of specimens, Portland cement mortars and concrete showed 35% higher compressive strength than pastes [88]. It is noticed that the pastes of alkali-activated material are resistant, but with extremely fragile ruptures. Because of this, it is believed that the insertion of fine aggregate in the pastes for the production of mortars provides an internal stress relief mechanism for alkali-activated material with EA, leading to higher compressive strengths.

3.2 Potential for degradation of methylene blue from mortars

Figure 12 shows the absorbance curves of methylene blue (MB) solutions collected after 24 hours in (a) dark and (b) UV-illuminated conditions, for the first test cycle. It is possible to observe a variation of the absorbance intensity at wavelengths of 292 nm and 664 nm as a function of the exposure of the solution to different mortars. The degradation of MB was monitored by measuring the decrease in absorbance of the peak at 664 nm [61,62,89]. The intensity of the absorption at the 664 nm peak decreased significantly with an increased content of alkaline activator, especially in relation to the step involving UV light; as such, it is believed that the solution was further discoloured due to a similar photocatalytic effect. Figure 13 shows the absorbance curves of the MB solutions collected after 24 hours in (a) dark and (b) UV-illuminated conditions in the second cycle. It is possible to observe that although the specimens were submitted to the test a second time, their MB-degradation potential increased. This indicates that the degradation is not simply induced by leaching or wash-out of alkalis from the pore fluid of the samples, which would be

24

expected to be much greater in the first than the second cycle, and therefore supports the discussion of a genuine catalytic effect in the MB degradation.

For the occurrence of photocatalytic effects semiconductor particles are necessary. Among the main semiconductor particles are: nano titanium dioxide photocatalyst, nano zinc oxide photocatalyst and ABO_3 type perovskite photocatalyst. Alkali-activated materials are perfect carrier of photocatalyst because of its unique 3D network structure [90]. $SrTiO_3$ is a typical structural diagram of ABO_3. In the structure of ABO_3, A site is alkali metal (IA group), alkaline earth metal (IIA group), and rare earth metal (IIIB group), respectively, while B site is transition metal. $NaTaO_3$ is another kind of typical ABO_3 perovskite, which has been considered as an efficient UV catalyst [90]. Despite having different structures and configurations from $SrTiO_3$ and $NaTaO_3$, the question that arises is whether pyrssonite ($Na_2Ca(CO_3) \cdot 2H_2O$) and thermonathrite ($Na_2CO_3 \cdot H_2O$) can present photocatalytic effects. Because they are phases present only in samples with better performance of organic dye degradation under UV lighting. Another important point to be highlighted is that the efficiency of the dye degradation is related to the combination of UV in the presence of SiO_2 [91]. In addition, pure SiO_2, in this case silica fume has a high percentage of SiO_2, is highly beneficial for photocatalytic improvement [92]. The fact that silica fume is smaller than 1 micron in size, for the high molarities 10M and 15M, many micro or nano particles of silica were free in the system and on the surface. Then, these nanoparticles are present as a point of photocatalysis and degradation of MB.
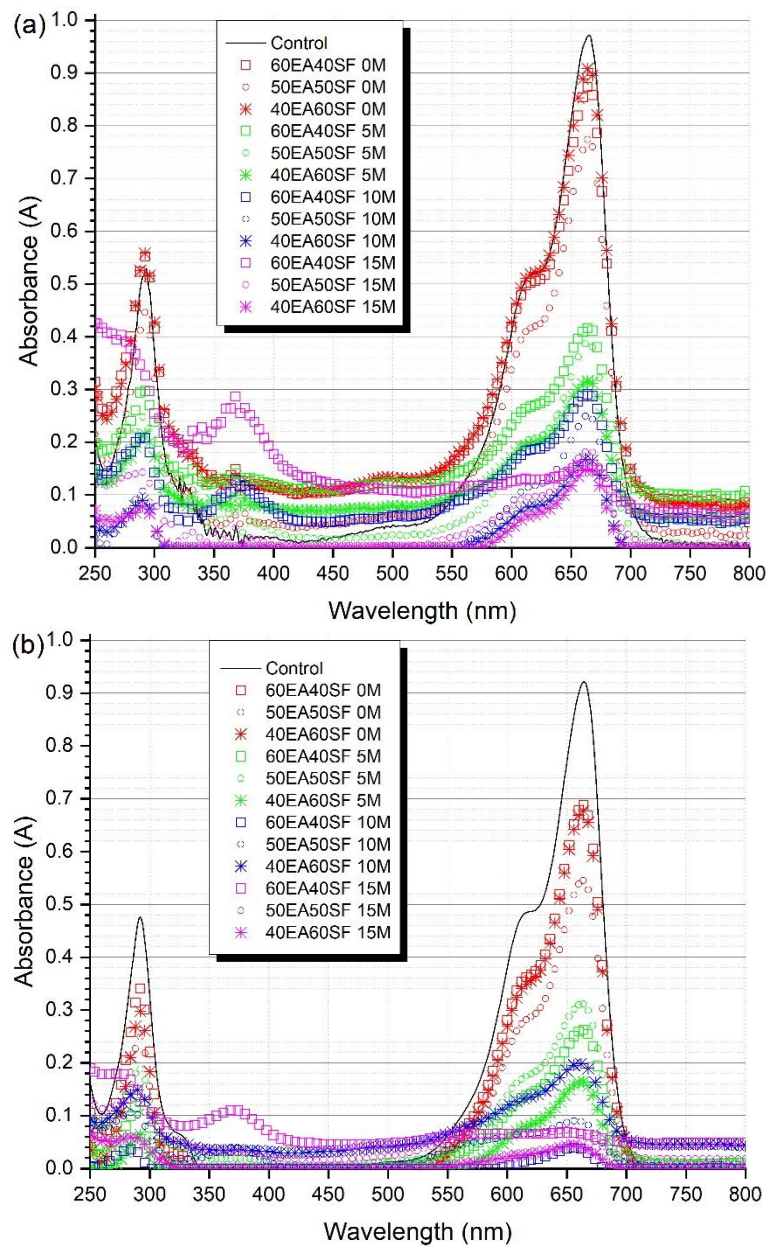
Fig. 12: (a) Absorbance curves in dark condition in the first cycle.
(b) Absorbance curves in illuminated condition in the first cycle.
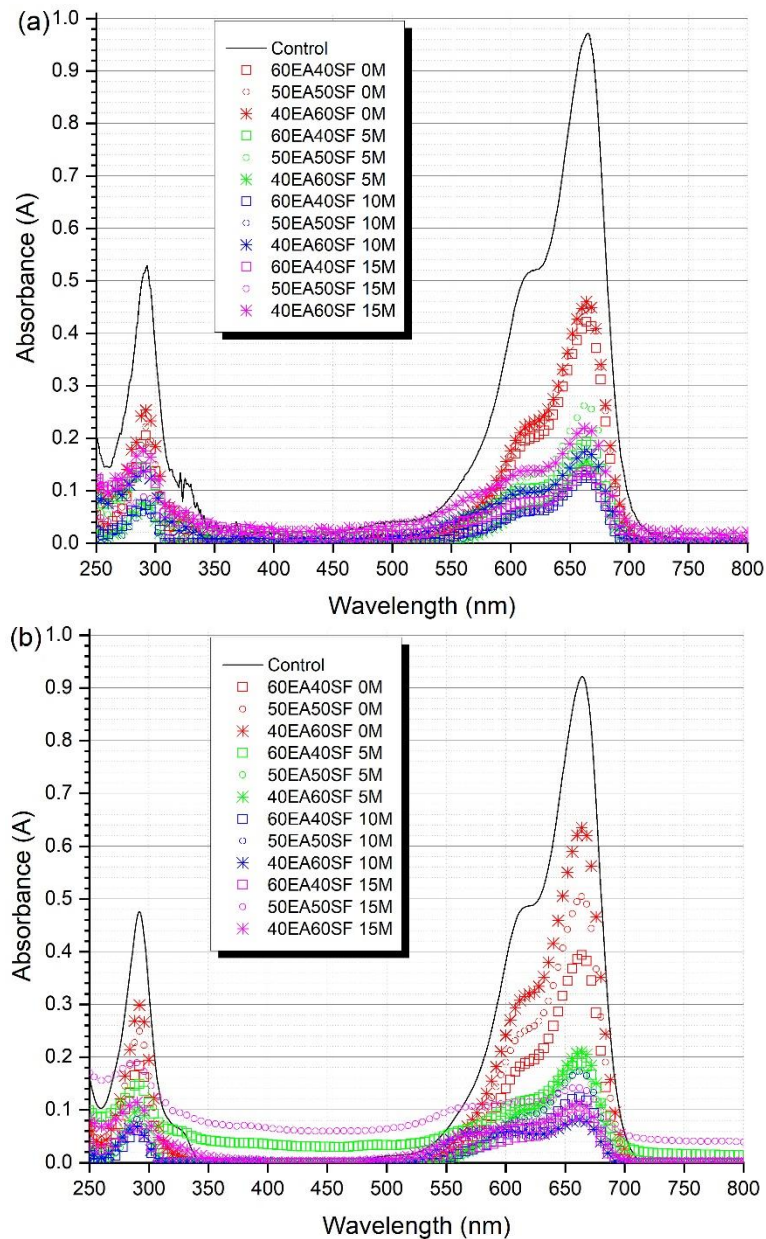
Fig. 13: (a) Absorbance curves in dark condition in the second cycle.
(b) Absorbance curves in illuminated condition in the second cycle.

Figure 14 shows the relationship between the concentrations of the MB solutions in contact with the mortar specimens, as a function of time (C) and initial concentration (C_o). In Figure 14 (a) it is possible to observe that the solutions with the mortar specimens displayed significant reductions of C/C_o in the dark conditions, especially with respect to mortars produced with sodium hydroxide. However, in Fig. 14 (b) it is possible to observe that the solutions with the mortar specimens showed higher decontamination in illuminated conditions, even after the specimens had already undergone 24 hours of adsorption in the dark. It should be highlighted that the initial MB concentrations in both dark and illuminated phases were the same. The

results obtained by the evaluation of the concentration of MB solutions collected after 4 hours of exposure to mortars can be seen. In the first four hours of exposure, MB removal quantities varying from 5.1 to 35.4% could be measured in the mortars subjected to dark conditions (without lighting). Contrary to expectations, mortars that presented greater water absorption by immersion, and pastes with higher pore volume and surface area, were not the ones responsible for the removal of higher levels of MB.

In the first four hours of exposure of the MB solution to the mortars in the illuminated condition (with UV light), removal of the MB quantities varying from 7.4 to 77.4% could be measured. With the exception of mortars 60EA40SF 0M and 40EA60SF 0M, all others presented larger reductions in the illuminated condition. By evaluating Figure 14, it is apparent that even after saturation in the MB solution for 24 hours under dark conditions (Fig 14a), the mortars in new solutions increased the speed and amount of MB removal during the UV-illuminated stage (Fig 14b), an indication that the UV light has fuelled the phenomenon of mortars 5, 10 and 15M, which removed up to 97% of the polluting dye (mortar 60EA40SF 10M).

For the second cycle of exposure of the mortars to the solutions, there was a further reduction of methylene blue concentrations, and it was possible to observe the removal of up to 86% for the dark condition and 92% for the illuminated condition (Fig 15).
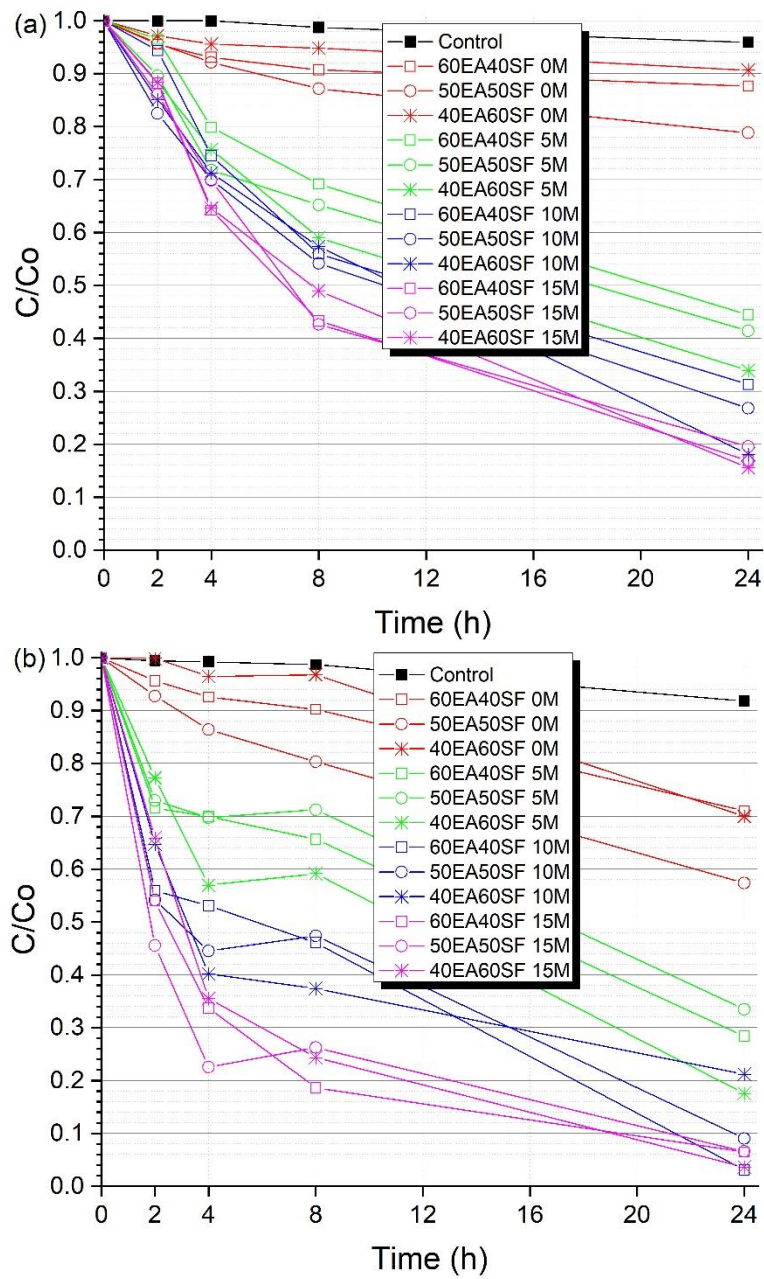
Fig. 14: Methylene blue concentration reduction by exposure to the mortars. (a) Dark condition in the first cycle. (b) Illuminated condition in the first cycle.
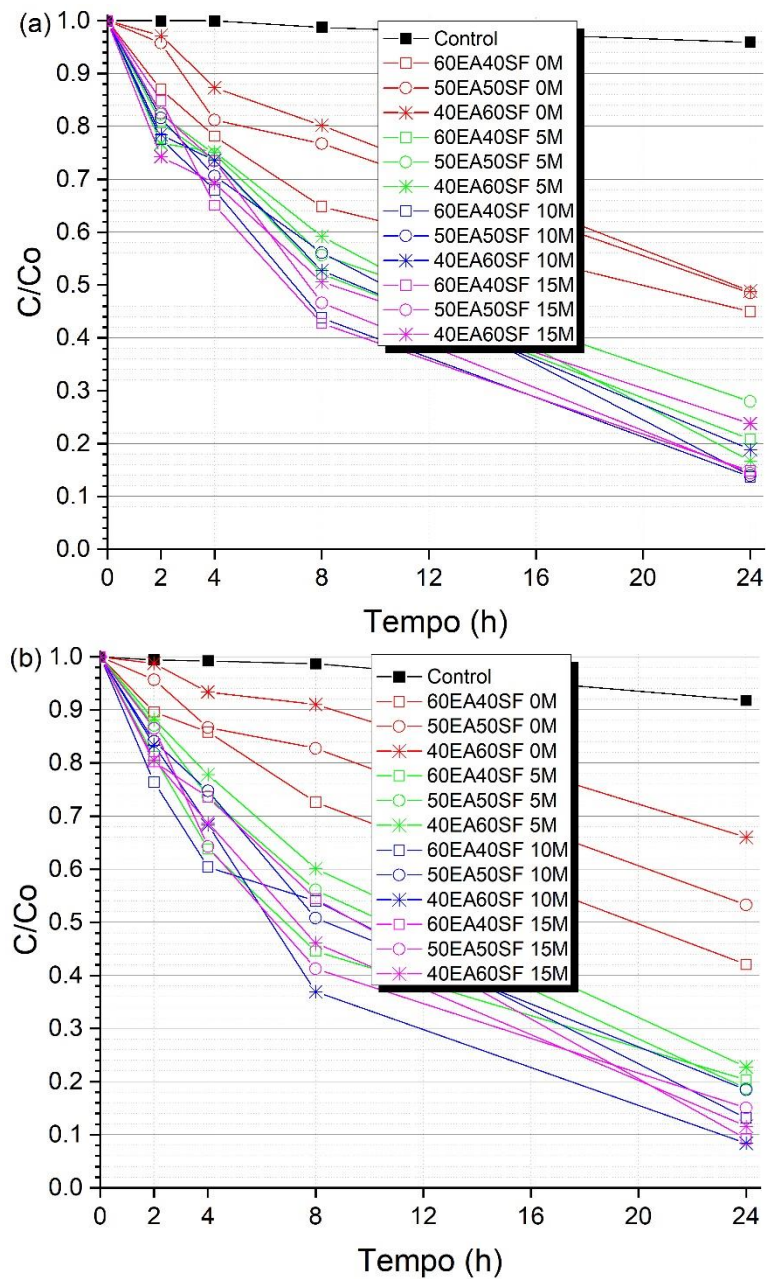
Fig. 15: Methylene blue concentration reduction by exposure to the mortars. (a) Dark condition in the second cycle. (b) Illuminated condition in the second cycle.

Tables 4 and 5 show the values leached of Al, Ca, Fe, Mg, K, and Na, in the methylene blue solutions after the first and second degradation cycles, respectively. The leached aluminum was below the limit of 0.2 mg/l [93–95], the leached iron was below the limit of 0.3 mg/l [93–95] and the sodium leached was above 200 mg/l [93,94] mainly for the proportions with 10 and 15M, which presented thermonatrite, a highly water-soluble sodium carbonate; it is worth noting that these limits are for assessing the quality of drinking water in Canada [93], and World Health Organization limits [95], or tap water in England and Wales [94].

30

Iron is one of the most abundant metals in Earth's crust. It is found in natural fresh waters at levels ranging from 0.5 to 50 mg/l [95]. The taste threshold concentration of sodium in water depends on the associated anion and the temperature of the solution [95]. At room temperature, the average taste threshold for sodium is about 200 mg/l [95]. No health-based guideline value has been derived, as the contribution from drinking-water to daily intake is small [95]. Potassium is an essential element in humans and is rarely, if ever, found in drinking-water at levels that could be a concern for healthy humans [95].

Table 4: Results of the solution analysis after the first cycle.

Condition	Solution of the mortar	[Al]	[Ca]	[Fe]	[Mg]	[K]	[Na]
				(mg/l or ppm)			
Dark	Control (without mortar)	< 0.05	0.85	< 0.10	< 0.25	0.43	5.61
	60EA40SF 0M	0.07	4.70	< 0.10	1.51	52.3	10.1
	50EA50SF 0M	< 0.05	6.24	0.14	1.09	33.4	8.21
	40EA60SF 0M	< 0.05	3.49	< 0.10	0.63	17.5	6.99
	60EA40SF 5M	< 0.05	1.23	< 0.10	0.32	69.1	154
	50EA50SF 5M	< 0.05	9.84	< 0.10	< 0.25	38.6	148
	40EA60SF 5M	< 0.05	2.63	< 0.10	< 0.25	31.5	149
	60EA40SF 10M	< 0.05	5.64	< 0.10	0.27	101	251
	50EA50SF 10M	< 0.05	14.5	< 0.10	0.36	83.2	261
	40EA60SF 10M	< 0.05	10.7	< 0.10	< 0.25	45.3	193
	60EA40SF 15M	< 0.05	3.49	< 0.10	0.29	206	407
	50EA50SF 15M	< 0.05	15.7	0.17	< 0.25	125	364
	40EA60SF 15M	< 0.05	22.3	< 0.10	0.35	160	455
Illuminated	Control (without mortar)	< 0.05	< 0.25	< 0.10	< 0.25	0.36	5.61
	60EA40SF 0M	< 0.05	9.38	< 0.10	4.27	142	17.0
	50EA50SF 0M	< 0.05	4.16	< 0.10	1.59	35.7	7.65
	40EA60SF 0M	< 0.05	2.59	< 0.10	0.71	5.34	5.94
	60EA40SF 5M	< 0.05	1.40	< 0.10	1.01	61.0	114
	50EA50SF 5M	< 0.05	5.48	< 0.10	0.86	9.70	55.7
	40EA60SF 5M	< 0.05	6.22	< 0.10	0.63	7.86	47.6
	60EA40SF 10M	< 0.05	3.24	< 0.10	0.71	84.0	201
	50EA50SF 10M	< 0.05	5.55	< 0.10	0.76	49.3	167
	40EA60SF 10M	< 0.05	6.24	< 0.10	0.36	26.8	160
	60EA40SF 15M	< 0.05	2.38	0.14	0.63	129	294
	50EA50SF 15M	< 0.05	6.25	< 0.10	0.54	71.2	249
	40EA60SF 15M	< 0.05	13.6	< 0.10	0.38	88.1	330

Table 5: Results of the solution analysis after the second cycle.

Condition	Solution of the mortar	[Al]	[Ca]	[Fe]	[Mg]	[K]	[Na]
					mg/L		
Dark	Control (without mortar)	< 0.05	0.38	< 0.10	< 0.25	< 0.25	4.43
	60EA40SF 0M	< 0.05	2.55	< 0.10	< 0.25	16.7	6.11
	50EA50SF 0M	< 0.05	2.48	< 0.10	< 0.25	15.9	7.27
	40EA60SF 0M	< 0.05	2.56	< 0.10	< 0.25	8.03	6.32
	60EA40SF 5M	< 0.05	0.88	< 0.10	< 0.25	21.3	65.4
	50EA50SF 5M	< 0.05	0.76	< 0.10	< 0.25	14.3	69.6
	40EA60SF 5M	< 0.05	0.78	< 0.10	< 0.25	17.0	98.6
	60EA40SF 10M	< 0.05	0.87	< 0.10	< 0.25	26.1	116
	50EA50SF 10M	< 0.05	1.16	< 0.10	< 0.25	18.1	103
	40EA60SF 10M	< 0.05	1.07	< 0.10	< 0.25	19.4	152
	60EA40SF 15M	< 0.05	1.40	< 0.10	< 0.25	32.0	215
	50EA50SF 15M	< 0.05	0.97	< 0.10	< 0.25	41.3	358
	40EA60SF 15M	< 0.05	3.29	< 0.10	< 0.25	44.0	444
Illuminated	Control (without mortar)	< 0.05	< 0.25	< 0.10	< 0.25	< 0.25	4.44
	60EA40SF 0M	< 0.05	3.17	< 0.10	< 0.25	17.2	6.42
	50EA50SF 0M	< 0.05	2.86	< 0.10	< 0.25	13.4	7.12
	40EA60SF 0M	< 0.05	2.15	< 0.10	< 0.25	5.34	4.85
	60EA40SF 5M	< 0.05	1.17	< 0.10	< 0.25	14.3	34.4
	50EA50SF 5M	< 0.05	1.00	< 0.10	< 0.25	8.40	32.7
	40EA60SF 5M	< 0.05	0.64	< 0.10	< 0.25	7.61	35.3
	60EA40SF 10M	< 0.05	0.85	< 0.10	< 0.25	14.6	54.8
	50EA50SF 10M	< 0.05	0.88	< 0.10	< 0.25	11.2	55.3
	40EA60SF 10M	< 0.05	1.25	< 0.10	0.26	14.5	99.3
	60EA40SF 15M	< 0.05	1.66	< 0.10	0.26	20.6	124
	50EA50SF 15M	< 0.05	1.09	< 0.10	< 0.25	32.7	280
	40EA60SF 15M	< 0.05	2.10	< 0.10	< 0.25	34.1	342

Four aspects must be highlighted:

(i) unlike other works found in the literature [89,96–98], in this work, agitation of the solution was not performed, thus reducing the speed of consumption of the dye;

(ii) the experiments were performed with mortars produced with sand that has low adsorption and is inert for the particle size used, so that only 25% of the mass of the specimen was constituted of paste with capacity to act in the phenomena described. Commonly, the works of the literature use pastes (without sand) instead of mortars;

(iii) also, different from the literature [96,98,99], this work evaluated the consumption of MB in two conditions, leading to higher dye consumption when the percentages of the dark and light

phases are added together. Some works in the literature perform these sequential steps without replacement of solution when transitioning from dark to UV stage;

(iv)   evaluation of the mortars was performed at an advanced age (240 days), once stabilisation of the main reactions had occurred, however, this is usually performed at less advanced ages (28 days).

4. Application feasibility and clean production

The results reflect the behavior of an alkali-activated material with potential application as mortars. The levels of mechanical strength of the mortars produced are compatible or superior to the mortars produced to evaluate the compressive strength of commercial Portland cement. The mechanical tests at the age of 154 days demonstrated the maintenance of the compressive strength of the mortars at advanced ages. This fact may be a good indication of the durability of the materials developed.

The results of porosity, water absorption, and apparent density were close to the results presented by alkali-activated mortars and Portland cement mortars. In these aspects, the produced alkali-activated mortars can have the same applications as usual Portland cement mortars, including structural applications, repair and as projected mortars. In addition, in the mortars with activator with a molarity of 15M, visually, an expressive expansion was noticed. This may indicate use as an expansive mortar. The high degradation potential of methylene blue presented by the produced alkali-activated mortars indicates the application as a wastewater depolluting material.

In addition to being used as a wastewater depollution material, the mortars produced use two by-products from other industrial processes. Currently, EA has no known commercial application and no economic value added. EA has a high content of unburned carbon in its composition and its insertion can generate carbon trapping in the alkali-activated matrix.

It is believed that this work was able to introduce alkali-activation as one of the means of assigning value to these materials. In addition, the application of materials produced in high specification activities such as water decontamination, and possibly as self-cleaning surfaces, may prove to be of great economic interest

in a world scenario that increasingly invests in clean technologies, and that seeks to maintain the sustainability of production processes.

The price of Portland cement in the Americas in 2020 was US$132/tonne [100]. Worldwide, the price of SF is US$150-800/tonne. However, in Brazil in December 2021, the active silica price was US$ 140/tonne. And in India, the price of SF is 67% of the price of Portland cement [101]. Considering that the mortars produced in this work had a maximum of 60% of the binder constituted by SF, and that EA still does not have added value, for noble applications it is believed to be viable the production of alkali-activated materials with SF and EA, even with the cost of activator.

In addition to the environmental and economic point of view, the present work contributes to the literature on the alkali-activation of high calcium systems. Since research in this field is still modest when compared to metakaolin or slag systems, the presentation of new results can encourage discussion and engagement of other researchers in this field.

5. Summary and conclusion

From the present work, it can be concluded that the EA produced by the burning of the eucalyptus chips in boilers for the production of steam and electric energy, presents higher levels of calcium content than many other biomass ashes found in the literature. In addition, the EA used here has a fine particle size and high specific surface area when milled, but a significant loss on ignition. The pastes produced with EA and SF presented C-S-H and C-A-S-H, with reduced intensity of peaks detected in the diffractograms when higher amounts of alkaline activator are added. Thus, EA and SF are reactive enough to form C-S-H and C-A-S-H without the need for alkaline activation; nonetheless, alkaline activation yielded greater formation of C-S-H in all pastes. The alkaline activation of pastes with 15M solution was shown to be expansive. The 5M pastes and mortars exhibited the best levels of compressive strength, corroborating the formation of C-S-H and C-A-S-H along with the absence of the expansion which was caused by hygroscopic gel formation in pastes activated with higher molarities. Alkaline activated mortars presented lower water absorption than mortars without activation. The mortars demonstrated the ability to decontaminate synthetic effluents based

on the high consumption of MB dye in both dark and UV-illuminated conditions; the consumption being significantly higher in illuminated conditions.

6. References

[1]   A.A. Myburg, D. Grattapaglia, G.A. Tuskan, U. Hellsten, R.D. Hayes, J. Grimwood, J. Jenkins, E. Lindquist, H. Tice, D. Bauer, D.M. Goodstein, I. Dubchak, A. Poliakov, E. Mizrachi, A.R.K. Kullan, S.G. Hussey, D. Pinard, K. Van Der Merwe, P. Singh, I. Van Jaarsveld, O.B. Silva-Junior, R.C. Togawa, M.R. Pappas, D.A. Faria, C.P. Sansaloni, C.D. Petroli, X. Yang, P. Ranjan, T.J. Tschaplinski, C.Y. Ye, T. Li, L. Sterck, K. Vanneste, F. Murat, M. Soler, H.S. Clemente, N. Saidi, H. Cassan-Wang, C. Dunand, C.A. Hefer, E. Bornberg-Bauer, A.R. Kersting, K. Vining, V. Amarasinghe, M. Ranik, S. Naithani, J. Elser, A.E. Boyd, A. Liston, J.W. Spatafora, P. Dharmwardhana, R. Raja, C. Sullivan, E. Romanel, M. Alves-Ferreira, C. Külheim, W. Foley, V. Carocha, J. Paiva, D. Kudrna, S.H. Brommonschenkel, G. Pasquali, M. Byrne, P. Rigault, J. Tibbits, A. Spokevicius, R.C. Jones, D.A. Steane, R.E. Vaillancourt, B.M. Potts, F. Joubert, K. Barry, G.J. Pappas, S.H. Strauss, P. Jaiswal, J. Grima-Pettenati, J. Salse, Y. Van De Peer, D.S. Rokhsar, J. Schmutz, The genome of Eucalyptus grandis, Nature. 510 (2014) 356–362. https://doi.org/10.1038/nature13308.

[2]   Indústria Brasileira de Árvores - IBÁ, Relatório Anual 2017, Brasília, 2017.

[3]   G. Zhao, Assessment of potential biomass energy production in China towards 2030 and 2050, Int. J. Sustain. Energy. 37 (2018) 47–66.

https://doi.org/10.1080/14786451.2016.1231677.

[4]   J. Rogelj, M. Den Elzen, N. Höhne, T. Fransen, H. Fekete, H. Winkler, R. Schaeffer, F. Sha, K. Riahi, M. Meinshausen, Paris Agreement climate proposals need a boost to keep warming well below 2 °c, Nature. 534 (2016) 631–639. https://doi.org/10.1038/nature18307.

[5]   G. Berndes, M. Hoogwijk, R. van den Broek, The contribution of biomass in the future global energy supply: a review of 17 studies, Biomass and Bioenergy. 25 (2003) 1–28. https://doi.org/10.1016/S0961-9534(02)00185-X.

[6]   M.A. da S. Miranda, G.B. de D. Ribeiro, S.R. Valverde, C. Isbaex, Eucalyptus sp. WOODCHIP POTENTIAL FOR INDUSTRIAL THERMAL ENERGY PRODUCTION1, Rev. Árvore. 41 (2017). https://doi.org/10.1590/1806-90882017000600004.

[7]   J. Kalembkiewicz, U. Chmielarz, Ashes from co-combustion of coal and biomass: New industrial wastes, Resour. Conserv. Recycl. 69 (2012) 109–121. https://doi.org/10.1016/j.resconrec.2012.09.010.

[8]   D.S. de Resende, H. Radispiel Filho, J.G. Keles, A.C. da Silva Bezerra, M.T. Paulino Aguilar, A.M.C. de Gouveia, Eucalyptus chip ashes in cementitious composites, Mater. Sci. Forum. 775–776 (2014) 205–209. https://doi.org/10.4028/www.scientific.net/MSF.775-776.205.

[9]   J.M. Paris, J.G. Roessler, C.C. Ferraro, H.D. Deford, T.G. Townsend, A review of waste products utilized as supplements to Portland cement in concrete, J. Clean. Prod. 121 (2016) 1–18. https://doi.org/10.1016/j.jclepro.2016.02.013.

[10]   J. Prasara-A, S.H. Gheewala, Sustainable utilization of rice husk ash from power plants: A

review, J. Clean. Prod. 167 (2017) 1020–1028. https://doi.org/10.1016/j.jclepro.2016.11.042.

[11]   G.C. Cordeiro, R.D. Toledo Filho, L.M. Tavares, E.M.R. Fairbairn, Experimental characterization of binary and ternary blended-cement concretes containing ultrafine residual rice husk and sugar cane bagasse ashes, Constr. Build. Mater. 29 (2012) 641–646. https://doi.org/10.1016/j.conbuildmat.2011.08.095.

[12]   F. Martirena, J. Monzó, Vegetable ashes as Supplementary Cementitious Materials, Cem. Concr. Res. 114 (2018) 57–64. https://doi.org/10.1016/j.cemconres.2017.08.015.

[13]   J.L. Provis, Alkali-activated materials, Cem. Concr. Res. 114 (2018) 40–48. https://doi.org/10.1016/j.cemconres.2017.02.009.

[14]   R. Patel, F. Kinney, G. Schumacher, Green Concrete Using 100% Fly Ash Based Hydraulic Binder, in: Int. Concr. Sustain. Conf., National Ready Mixed Concrete Association, Seatle, 2012: p. 15.

[15]   D. Cross, J. Stephens, J. Vollmer, Structural Applications of 100 Percent Fly Ash Concrete, 2005 World Coal Ash. (2005) 1–19.

[16]   O. Wan-En, L. Yun-Ming, H. Cheng-Yong, M.M.A.B. Abdullah, L.Y. Li, L.N. Ho, F.K. Loong, O. Shee-Ween, N. Hui-Teng, N. Yong-Sing, N.A. Jaya, Comparative mechanical and microstructural properties of high calcium fly ash one-part geopolymers activated with Na2SiO3-anhydrous and NaAlO2, J. Mater. Res. Technol. 15 (2021) 3850–3866. https://doi.org/10.1016/j.jmrt.2021.10.018.

[17]   K. Ruengsillapanun, T. Udtaranakron, T. Pulngern, W. Tangchirapat, C. Jaturapitakkul, Mechanical properties, shrinkage, and heat evolution of alkali activated fly ash concrete,

Constr.   Build.   Mater.   299   (2021)   123954.
https://doi.org/10.1016/j.conbuildmat.2021.123954.

[18]   S. Hanjitsuwan, B. Injorhor, T. Phoo-ngernkham, N. Damrongwiriyanupap, L.Y. Li, P. Sukontasukkul, P. Chindaprasirt, Drying shrinkage, strength and microstructure of alkali-activated high-calcium fly ash using FGD-gypsum and dolomite as expansive additive, Cem.   Concr.   Compos.   114   (2020)   103760. https://doi.org/10.1016/j.cemconcomp.2020.103760.

[19]   Saloni, Parveen, Y.Y. Lim, T.M. Pham, Jatin, J. Kumar, Sustainable alkali activated concrete with fly ash and waste marble aggregates: Strength and Durability studies, Constr. Build. Mater. 283 (2021). https://doi.org/10.1016/j.conbuildmat.2021.122795.

[20]   P. Chindaprasirt, B. Sriopas, P. Phosri, P. Yoddumrong, K. Anantakarn, W. Kroehong, Hybrid high calcium fly ash alkali-activated repair material for concrete exposed to sulfate environment, J. Build. Eng. 45 (2022) 103590. https://doi.org/10.1016/j.jobe.2021.103590.

[21]   T. Phoo-ngernkham, C. Phiangphimai, D. Intarabut, S. Hanjitsuwan, N. Damrongwiriyanupap, L. yuan Li, P. Chindaprasirt, Low cost and sustainable repair material made from alkali-activated high-calcium fly ash with calcium carbide residue, Constr.   Build.   Mater.   247   (2020)   118543. https://doi.org/10.1016/j.conbuildmat.2020.118543.

[22]   P. Chindaprasirt, T. Boonbamrung, A. Poolsong, W. Kroehong, Effect of elevated temperature on polypropylene fiber reinforced alkali-activated high calcium fly ash paste, Case Stud. Constr. Mater. 15 (2021) e00554. https://doi.org/10.1016/j.cscm.2021.e00554.

[23]   T. Chompoorat, T. Thepumong, P. Nuaklong, P. Jongvivatsakul, S. Likitlersuang, Alkali-

Activated Controlled Low-Strength Material Utilizing High-Calcium Fly Ash and Steel Slag for Use as Pavement Materials, J. Mater. Civ. Eng. 33 (2021) 04021178. https://doi.org/10.1061/(asce)mt.1943-5533.0003798.

[24] A.H.C. Teixeira, P.R.R.S. Junior, T.H. Silva, R.R. Barreto, A.C. da Silva Bezerra, Low-carbon concrete based on binary biomass ash-silica fume binder to produce eco-friendly paving blocks, Materials (Basel). 13 (2020) 1534. https://doi.org/10.3390/ma13071534.

[25] A.C. da S. Bezerra, S. França, L.F. de Magalhães, M.C.R. de Carvalho, Alkaline activation of high-calcium ash and iron ore tailings and their recycling potential in building materials, Ambient. Construído. 19 (2019) 99–112. https://doi.org/10.1590/s1678-86212019000300327.

[26] J. Lee, T. Lee, J. Jeong, J. Jeong, Mix design optimization and environmental impact assessment of low-carbon materials containing alkali-activated slag and high CaO fly ash, Constr. Build. Mater. 267 (2021) 120932. https://doi.org/10.1016/j.conbuildmat.2020.120932.

[27] W.G. Valencia-Saavedra, A.M. Aguirre-Guerrero, R. Mejía de Gutiérrez, Alkali-activated concretes based on high unburned carbon content fly ash: carbonation and corrosion performance, Eur. J. Environ. Civ. Eng. 0 (2020) 1–21. https://doi.org/10.1080/19648189.2020.1785948.

[28] K.L.L. Scrivener, E.M.M. Gartner, V.M. John, E.M.M. Gartner, Eco-efficient cements: Potential economically viable solutions for a low-CO2 cement-based materials industry, Cem. Concr. Res. 114 (2018) 2–26. https://doi.org/10.1016/j.cemconres.2018.03.015.

[29] A.C.A. Muller, K.L. Scrivener, J. Skibsted, A.M. Gajewicz, P.J. McDonald, Influence of

silica fume on the microstructure of cement pastes: New insights from 1H NMR relaxometry, Cem. Concr. Res. 74 (2015) 116–125. https://doi.org/10.1016/j.cemconres.2015.04.005.

[30]   H. Cheng-yi, R.F. Feldman, Influence of silica fume on the microstructural development in cement mortars, Cem. Concr. Res. 15 (1985) 285–294. https://doi.org/10.1016/0008-8846(85)90040-7.

[31]   P.K. Mehta, O.E. Gjørv, Properties of portland cement concrete containing fly ash and condensed silica-fume, Cem. Concr. Res. 12 (1982) 587–595. https://doi.org/10.1016/0008-8846(82)90019-9.

[32]   U.S.G. Survey, Mineral commodity summaries 2022, 2022. https://doi.org/10.3133/mcs2022.

[33]   L.N. Sousa, P.F. Figueiredo, S. França, M.V. de Moura Solar Silva, P.H.R. Borges, A.C. da S. Bezerra, Effect of Non-Calcined Sugarcane Bagasse Ash as an Alternative Precursor on the Properties of Alkali-Activated Pastes, Molecules. 27 (2022) 1185. https://doi.org/10.3390/molecules27041185.

[34]   ASTM, C618 - 19 Standard Specification for Coal Fly Ash and Raw or Calcined Natural Pozzolan for Use in Concrete, ASTM International, West Conshohocken, PA, ASTM Int. West Conshohocken, PA. (2019).

[35]   A.C. da S. Bezerra, S.L.C. Saraiva, L.F. dos S. Lara, L.W.A. de Castro, R.C. Gomes, C. de S. Rodrigues, M.C.N.F. Ferreira, M.T.P. Aguilar, Effect of partial replacement with thermally processed sugar cane bagasse on the properties of mortars, Rev. Mater. 22 (2017) e11785. https://doi.org/10.1590/S1517-707620170001.0117.

[36] J.C. Benezet, A. Benhassaine, The influence of particle size on the pozzolanic reactivity of quartz powders, Powder Technol. 103 (1999) 26–29. https://doi.org/10.1016/S0032-5910(99)00010-8.

[37] E. Zolotoyabko, E.N. Caspi, J.S. Fieramosca, R.B. Von Dreele, F. Marin, G. Mor, L. Addadi, S. Weiner, Y. Politi, Differences between Bond Lengths in Biogenic and Geological Calcite, Cryst. Growth Des. 10 (2010) 1207–1214. https://doi.org/10.1021/cg901195t.

[38] M.C. Verbraeken, E. Suard, J.T.S. Irvine, Structural and electrical properties of calcium and strontium hydrides, J. Mater. Chem. 19 (2009) 2766. https://doi.org/10.1039/b820173k.

[39] J. Zhang, Effect of pressure on the thermal expansion of MgO up to 8.2 GPa, Phys. Chem. Miner. 27 (2000) 145–148. https://doi.org/10.1007/s002690050001.

[40] D. Walker, P.K. Verma, L.M.D. Cranswick, R.L. Jones, S.M. Clark, S. Buhre, Halite-sylvite thermoelasticity, Am. Mineral. 89 (2004) 204–210. https://doi.org/10.2138/am-2004-0124.

[41] O. Chaix-Pluchery, J. Pannetier, J. Bouillot, J.C. Niepce, Structural prereactional transformations in Ca(OH)2, J. Solid State Chem. 67 (1987) 225–234. https://doi.org/10.1016/0022-4596(87)90358-6.

[42] H. Braekken, Zur Kristallstruktur des kubischen Karborunds, Zeitschrift Für Krist. 75 (1930) 572–573.

[43] S. Stefanoski, M.C. Blosser, G.S. Nolas, Pressure Effects on the Size of Type-I and Type-II Si-Clathrates Synthesized by Spark Plasma Sintering, Cryst. Growth Des. 13 (2013) 195–197. https://doi.org/10.1021/cg3013443.

[44] J. Bhatty, K. Reid, D. Dollimore, G. Gamlen, R. Mangabhai, P. Rogers, T. Shah, The Derivation of Kinetic Parameters in Analysis of Portland Cement for Portlandite and Carbonate by Thermogravimetry, in: Compos. Anal. by Thermogravim., ASTM International, 100 Barr Harbor Drive, PO Box C700, West Conshohocken, PA 19428-2959, PO Box C700, West Conshohocken, PA 19428-2959, 2009: pp. 204-204–12. https://doi.org/10.1520/stp26408s.

[45] D. Hourlier, Thermal decomposition of calcium oxalate: beyond appearances, J. Therm. Anal. Calorim. 136 (2019) 2221–2229. https://doi.org/10.1007/s10973-018-7888-1.

[46] J. Fromm, Wood formation of trees in relation to potassium and calcium nutrition, Tree Physiol. 30 (2010) 1140–1147. https://doi.org/10.1093/treephys/tpq024.

[47] M. Usman, A.Y. Khan, S.H. Farooq, A. Hanif, S. Tang, R.A. Khushnood, S.A. Rizwan, Eco-friendly self-compacting cement pastes incorporating wood waste as cement replacement: A feasibility study, J. Clean. Prod. 190 (2018) 679–688. https://doi.org/10.1016/j.jclepro.2018.04.186.

[48] R.M.R.O. MENEZES, R.M. DA SILVA, E.P. FIGUEIREDO, A.C.D.S. BEZERRA, M.T.P. AGUILAR, P.R. CETLIN, Hydraulic binder obtained from recycled cement and sand powder, Rev. IBRACON Estruturas e Mater. 11 (2018) 1178–1185. https://doi.org/10.1590/s1983-41952018000600003.

[49] J. Skocek, M. Zajac, M. Ben Haha, Carbon Capture and Utilization by mineralization of cement pastes derived from recycled concrete, Sci. Rep. 10 (2020) 1–12. https://doi.org/10.1038/s41598-020-62503-z.

[50] M. Záleská, Z. Pavlík, M. Pavlíková, L. Scheinherrová, J. Pokorný, A. Trník, P. Svora, J.

Fořt, O. Jankovský, Z. Suchorab, R. Černý, Biomass ash-based mineral admixture prepared from municipal sewage sludge and its application in cement composites, Clean Technol. Environ. Policy. 20 (2018) 159–171. https://doi.org/10.1007/s10098-017-1465-3.

[51] G.B. Denari, E.T.G. Cavalheiro, Princípios e aplicações de análise térmica, (2012) 40.

[52] J.L. Perez-Rodriguez, A. Duran, M.A. Centeno, J.M. Martinez-Blanes, M.D. Robador, Thermal analysis of monument patina containing hydrated calcium oxalates, Thermochim. Acta. 512 (2011) 5–12. https://doi.org/10.1016/j.tca.2010.08.015.

[53] N.V.Y. Scarlett, I.C. Madsen, Quantification of phases with partial or no known crystal structures, Powder Diffr. 21 (2006) 278–284. https://doi.org/10.1154/1.2362855.

[54] C. Naber, S. Stegmeyer, D. Jansen, F. Goetz-Neunhoeffer, J. Neubauer, The PONKCS method applied for time resolved XRD quantification of supplementary cementitious material reactivity in hydrating mixtures with ordinary Portland cement, Constr. Build. Mater. 214 (2019) 449–457. https://doi.org/10.1016/j.conbuildmat.2019.04.157.

[55] S.T. Bergold, F. Goetz-Neunhoeffer, J. Neubauer, Quantitative analysis of C–S–H in hydrating alite pastes by in-situ XRD, Cem. Concr. Res. 53 (2013) 119–126. https://doi.org/10.1016/j.cemconres.2013.06.001.

[56] E. Bonaccorsi, S. Merlino, A.R. Kampf, The crystal structure of tobermorite 14 Å (plombierite), a C-S-H phase, J. Am. Ceram. Soc. 88 (2005) 505–512. https://doi.org/10.1111/j.1551-2916.2005.00116.x.

[57] NBR 9778, NBR9778: Argamassa e concreto endurecidos - Determinação da absorção de água, índice de vazios e massa específica, (2009).

[58] L.F. de Magalhães, S. França, M. dos S. Oliveira, R.A.F. Peixoto, S.A.L. Bessa, A.C. da S. Bezerra, Iron ore tailings as a supplementary cementitious material in the production of pigmented cements, J. Clean. Prod. 274 (2020) 123260. https://doi.org/10.1016/j.jclepro.2020.123260.

[59] ABNT, NBR 7215 -Cimento Portland - Determinação da resistência à compressão, (2019).

[60] A.C. da S. Bezerra, M.T.P. Aguilar, P.R. Cetlin, The influence of specimen capping on the results of compression strength tests of cementitious composites, Rev. Esc. Minas. 65 (2012) 291–295. https://doi.org/10.1590/S0370-44672012000300003.

[61] J.M. De la Rosa, A.Z. Miller, J.S. Pozo-Antonio, J.A. González-Pérez, N.T. Jiménez-Morillo, A. Dionisio, Assessing the effects of UVA photocatalysis on soot-coated TiO2-containing mortars, Sci. Total Environ. 605–606 (2017) 147–157. https://doi.org/10.1016/j.scitotenv.2017.06.127.

[62] T. Larbi, M.A. Amara, B. Ouni, M. Amlouk, Enhanced photocatalytic degradation of methylene blue dye under UV-sunlight irradiation by cesium doped chromium oxide thin films, Mater. Res. Bull. 95 (2017) 152–162. https://doi.org/10.1016/j.materresbull.2017.07.024.

[63] F. Shaqour, M. Ismeik, M. Esaifan, Alkali activation of natural clay using a Ca(OH)2/Na2CO3 alkaline mixture, Clay Miner. 52 (2017) 485–496. https://doi.org/10.1180/claymin.2017.052.4.06.

[64] S.A. Bernal, Microstructural Changes Induced by CO2 Exposure in Alkali-Activated Slag/Metakaolin Pastes, Front. Mater. 3 (2016). https://doi.org/10.3389/fmats.2016.00043.

[65] S.A. Bernal, R. San Nicolas, J.L. Provis, R. Mejía de Gutiérrez, J.S.J. van Deventer, Natural

carbonation of aged alkali-activated slag concretes, Mater. Struct. 47 (2013) 693–707. https://doi.org/10.1617/s11527-013-0089-2.

[66] S.A. Bernal, J.L. Provis, A. Fernández-Jiménez, P. V Krivenko, E. Kavalerova, M. Palacios, C. Shi, Binder Chemistry – High-Calcium Alkali-Activated Materials, in: Alkali Act. Mater., Springer Netherlands, 2014: pp. 59–91. https://doi.org/10.1007/978-94-007-7672-2_3.

[67] S.A. Bernal, J.L. Provis, D.G. Brice, A. Kilcullen, P. Duxson, J.S.J. van Deventer, Accelerated carbonation testing of alkali-activated binders significantly underestimates service life: The role of pore solution chemistry, Cem. Concr. Res. 42 (2012) 1317–1326. https://doi.org/10.1016/j.cemconres.2012.07.002.

[68] E. Prud'homme, P. Michaud, E. Joussein, C. Peyratout, A. Smith, S. Rossignol, In situ inorganic foams prepared from various clays at low temperature, Appl. Clay Sci. 51 (2011) 15–22. https://doi.org/10.1016/j.clay.2010.10.016.

[69] A. Bonilla, M.A. Villaquirán-Caicedo, R.M. de Gutiérrez, Novel Alkali-Activated Materials with Photocatalytic and Bactericidal Properties Based on Ceramic Tile Waste, Coatings. 12 (2022). https://doi.org/10.3390/coatings12010035.

[70] H. Choi, H. Choi, M. Inoue, R. Sengoku, Control of the Polymorphism of Calcium Carbonate Produced by Self-Healing in the Cracked Part of Cementitious Materials, Appl. Sci. 7 (2017) 546. https://doi.org/10.3390/app7060546.

[71] K. Mohammed Haneefa, S. Divya Rani, R. Ramasamy, M. Santhanam, Microstructure and geochemistry of lime plaster mortar from a heritage structure, Constr. Build. Mater. 225 (2019) 538–554. https://doi.org/10.1016/j.conbuildmat.2019.07.159.

[72] B. Suryanto, J.O. Buckman, P. Thompson, M. Bolbol, W.J. McCarter, Monitoring micro-crack healing in an engineered cementitious composite using the environmental scanning electron microscope, Mater. Charact. 119 (2016) 175–185. https://doi.org/10.1016/j.matchar.2016.07.021.

[73] S. Diamond, The microstructure of cement paste and concrete—a visual primer, Cem. Concr. Compos. 26 (2004) 919–933. https://doi.org/10.1016/j.cemconcomp.2004.02.028.

[74] S. Jia, I.G. Richardson, Micro- and nano-structural evolutions in white Portland cement/pulverized fuel ash cement pastes due to deionized-water leaching, Cem. Concr. Res. 103 (2018) 191–203. https://doi.org/10.1016/j.cemconres.2017.10.014.

[75] D.C.S. Garcia, M.M.N. de S. Soares, A.C. da S. Bezerra, M.T.P. Aguilar, R.B. Figueiredo, Microstructure and hardness of cement pastes with mineral admixture, Rev. Mater. 22 (2017). https://doi.org/10.1590/S1517-707620170002.0145.

[76] B. Singh, Rice husk ash, in: Waste Suppl. Cem. Mater. Concr., Elsevier, 2018: pp. 417–460. https://doi.org/10.1016/B978-0-08-102156-9.00013-4.

[77] M.A. Villaquirán-Caicedo, R. Mejía de Gutiérrez, Comparison of different activators for alkaline activation of construction and demolition wastes, Constr. Build. Mater. 281 (2021). https://doi.org/10.1016/j.conbuildmat.2021.122599.

[78] S. França, M.V. de Moura Solar Silva, P.H. Ribeiro Borges, A.C. da Silva Bezerra, A review on some properties of alkali-activated materials, Innov. Infrastruct. Solut. 7 (2022). https://doi.org/10.1007/s41062-022-00789-w.

[79] V. Yogendran, B.W. Langan, M.A. Ward, Hydration of cement and silica fume paste, Cem. Concr. Res. 21 (1991) 691–708. https://doi.org/10.1016/0008-8846(91)90164-d.

[80] G. Huang, K. Yang, Y. Sun, Z. Lu, X. Zhang, L. Zuo, Y. Feng, R. Qian, Y. Qi, Y. Ji, Z. Xu, Influence of NaOH content on the alkali conversion mechanism in MSWI bottom ash alkali-activated mortars, Constr. Build. Mater. 248 (2020) 118582. https://doi.org/10.1016/j.conbuildmat.2020.118582.

[81] M.C. Bignozzi, S. Manzi, M.E. Natali, W.D.A. Rickard, A. Van Riessen, Room temperature alkali activation of fly ash: The effect of Na 2O/SiO2 ratio, Constr. Build. Mater. 69 (2014) 262–270. https://doi.org/10.1016/j.conbuildmat.2014.07.062.

[82] Z. Bayer Öztürk, İ.İ. Atabey, Mechanical and microstructural characteristics of geopolymer mortars at high temperatures produced with ceramic sanitaryware waste, Ceram. Int. (2022). https://doi.org/10.1016/j.ceramint.2022.01.166.

[83] D.H. Vo, C.L. Hwang, K.D. Tran Thi, M.C. Liao, M.D. Yehualaw, Engineering performance of high-content MgO-Alkali-activated slag mortar incorporating fine recycled concrete aggregate and fly ash, J. Mater. Cycles Waste Manag. 23 (2021) 778–789. https://doi.org/10.1007/s10163-020-01171-7.

[84] M. Lorena Figueiredo Martins, P. Roberto Ribeiro Soares Junior, T. Henrique da Silva, P. de Souza Maciel, I. Peixoto Pinheiro, A. Cesar da Silva Bezerra, Magnesium industry waste and red mud to eco-friendly ternary binder: Producing more sustainable cementitious materials, Constr. Build. Mater. 310 (2021) 125172. https://doi.org/10.1016/J.CONBUILDMAT.2021.125172.

[85] Associação Brasileira de Normas Técnicas (ABNT), NBR 16697 - Cimento Portland - Requisitos, Associação Brasileira de Normas Técnicas, Brazil, 2018.

[86] ASTM International, C1157 - Standard Performance Specification for Hydraulic Cement,

ASTM International, United States, 2017. https://doi.org/10.1520/C1157.

[87] M. Klun, V. Bosiljkov, V. Bokan-Bosiljkov, The relation between concrete, mortar and paste scale early age properties, Materials (Basel). 14 (2021). https://doi.org/10.3390/ma14061569.

[88] X. Chen, S. Wu, J. Zhou, Experimental and modeling study of dynamic mechanical properties of cement paste, mortar and concrete, Constr. Build. Mater. 47 (2013) 419–430. https://doi.org/10.1016/j.conbuildmat.2013.05.063.

[89] L. Chen, K. Zheng, Y. Liu, Geopolymer-supported photocatalytic TiO2 film: Preparation and characterization, Constr. Build. Mater. 151 (2017) 63–70. https://doi.org/10.1016/j.conbuildmat.2017.06.097.

[90] Y. Wang, N. Zhang, Y. Zhou, C. Li, J. Zhao, Y. Zhang, Photocatalysis in alkali activated cementitious materials, J. Build. Eng. 46 (2022) 103749. https://doi.org/10.1016/j.jobe.2021.103749.

[91] A.I. Biradar, P.D. Sarvalkar, S.B. Teli, C.A. Pawar, P.S. Patil, N.R. Prasad, Photocatalytic degradation of dyes using one-step synthesized silica nanoparticles, Mater. Today Proc. 43 (2020) 2832–2838. https://doi.org/10.1016/j.matpr.2020.11.946.

[92] D. Benz, H. Van Bui, H.T. Hintzen, M.T. Kreutzer, J.R. van Ommen, Mechanistic insight into the improved photocatalytic degradation of dyes for an ultrathin coating of SiO2 on TiO2 (P25) nanoparticles, Chem. Eng. J. Adv. 10 (2022). https://doi.org/10.1016/j.ceja.2022.100288.

[93] Health Canada, Guidelines for Canadian Drinking Water Quality Summary Table Federal-Provincial-Territorial Committee on Drinking Water of the Federal-Provincial-Territorial

Committee on Health and the Environment, Ottawa, ON, Canada, 2019.

[94] Water - England and Wales, The Water Supply (Water Quality) Regulations 2018, (2018).

[95] J.A. Cotruvo, 2017 WHO Guidelines for Drinking Water Quality: First Addendum to the Fourth Edition, J. Am. Water Works Assoc. 109 (2017) 44–51. https://doi.org/10.5942/jawwa.2017.109.0087.

[96] A.P. Heitmann, P.S.O. Patrício, I.R. Coura, E.F. Pedroso, P.P. Souza, H.S. Mansur, A. Mansur, L.C.A. Oliveira, Nanostructured niobium oxyhydroxide dispersed Poly (3-hydroxybutyrate) (PHB) films: Highly efficient photocatalysts for degradation methylene blue dye, Appl. Catal. B Environ. 189 (2016) 141–150. https://doi.org/10.1016/j.apcatb.2016.02.031.

[97] T.R. Giraldi, J.P. Swerts, M.A. Vicente, V.R. de Mendonça, E.C. Paris, C. Ribeiro, Utilização de partículas de ZnO:Mn para a degradação do azul de metileno por processo de fotocatálise, Cerâmica. 62 (2016) 345–350. https://doi.org/10.1590/0366-69132016623642000.

[98] H. Atout, M.G. Álvarez, D. Chebli, A. Bouguettoucha, D. Tichit, J. Llorca, F. Medina, Enhanced photocatalytic degradation of methylene blue: Preparation of TiO2/reduced graphene oxide nanocomposites by direct sol-gel and hydrothermal methods, Mater. Res. Bull. 95 (2017) 578–587. https://doi.org/10.1016/j.materresbull.2017.08.029.

[99] M.A.N.S. Moreira, A.P. Heitmann, A.C.S. Bezerra, P.S.O. Patrício, L.C.A. de Oliveira, C.S. Castro, P.P. de Souza, Photocatalytic performance of cementitious materials with addition of red mud and Nb2O5 particles, Constr. Build. Mater. 259 (2020) 119851. https://doi.org/10.1016/j.conbuildmat.2020.119851.

[100] Sindicato Nacional da Industria de Cimento, Annual Report 2020, Sindicato Nacional da Industria de Cimento, São Paulo, Brazil, 2020. http://www.snic.org.br/pdf/RelatorioAnual2013final.pdf.

[101] R. Bajpai, K. Choudhary, A. Srivastava, K.S. Sangwan, M. Singh, Environmental impact assessment of fly ash and silica fume based geopolymer concrete, J. Clean. Prod. 254 (2020) 120147. https://doi.org/10.1016/j.jclepro.2020.120147.